MoonIndex, an Open-Source Tool to Generate Spectral Indexes for the Moon from M^3 Data

Javier Eduardo Suárez-Valencia[1], Angelo Pio Rossi[1], Francesca Zambon[2], Cristian Carli[2], and Giacomo Nodjoumi[1]

[1]School of Science, Constructor University, Bremen, Germany, [2]INAF-Istituto Nazionale di Astrofisica, Italy.

Corresponding author: Javier Eduardo Suárez Valencia (jsuarezvalencia@constructor.university)

This manuscript is a non-peer reviewed preprint of an article submitted to the journal Earth and Space Science.

Abstract

Spectral indexes are tools widely used to analyze the composition of the lunar surface. Many indexes have been formulated over the years, but there is no unified database for them. In this work we describe an Open-Source Python package called ***MoonIndex***, that recreates thirty-nine indexes compiled from the literature and derived from several instruments, using data from the Moon Mineralogy Mapper (M^3). The processing started with the filtration of the data cubes to reduce the noise, the continuum of the spectrum was then removed using the convex hull and linear-fit methods. Later, the indexes were calculated, following as possible the original formulations. The results on spectral indexes calculated on the original spectra were similar to those already published. Conversely, the results obtained for spectral indexes calculated after the continual removal were not always coherent, some indexes, like the band depth, are especially sensitive to the removal method, as well as the derived band areas and asymmetries. We also recreated RGB composite maps, our results highlight the compositional patterns is a similar way as the ones in the literature, even if the color ramps can differ. The products of ***MoonIndex*** are open, ready for interpretation, versatile, consistent, and cross-comparable.

Plain Language Summary

Spectral indexes are parameters defined from the characteristics of reflectance spectrums, and they are useful to investigate the spectral properties of a surface and to retrieve mineralogical properties of a planetary body. They can reveal the presence of specific minerals in rocks, indicate mineralogical variations from different units, highlight physical properties of a surface, or show the effect of the exposure to the space environment. For the Moon, several spectral indexes have been formulated over time using data from many spacecrafts, but no unified database is available. In this work, we created an open-source Python package called M***oonIndex***, which recreates thirty-nine indexes to study the lunar surface. The indexes were collected from the literature, and our results achieved various levels of fidelity. Some of the indexes we calculated are exactly reproducing those found in the literature, while in other cases, index calculations differ due to processing constraints or due to missing information in the original formulations, such as the continuum removal method used, or the band operations conducted to create the indexes. ***MoonIndex*** is a reliable and versatile tool to approach the compositional analysis of the lunar surface.

1 Introduction

The surface of the Moon has a constrained mineralogical diversity, it has been broadly divided into two types of terrains, the “highlands” which are anorthositic-rich and relatively light, and “maria”, effusive plains enriched in mafic and opaque minerals (Taylor, 1976, Hiesinger and Head, 2006). In the highlands, the dominant minerals are calcium plagioclases (Taylor, 1972, Warren and Korotev, 2022), while in the maria mafic compositions become important showing higher abundances of clinopyroxene (CPX), orthopyroxene (OPX), and olivine (Agrell et al., 1970, Albee, 2003). The clear definition of the lunar mineralogy has been driven by the samples returned by space missions (Prissel and Prissel, 2021), but due to their limited coverage of the lunar surface, the use of remote sensing techniques is still the only way to assess the mineralogy of the Moon at a regional level. In this respect, the formulation and use of spectral indexes is a straightforward way to approach and visualize the mineralogical diversity of the Moon. In this study we present ***MoonIndex***, an open-source tool to generate several spectral

indexes derived from the data of the Moon Mineralogy Mapper (M^3). Mineralogical exploration of the Moon.

After the end of the Apollo missions, the exploration of the Moon shifted towards the use of remote sensing spacecrafts around the Moon. These orbiters allowed global and long-lasting surveys of the surface, including the study of mineralogical and elemental variations across lunar terrains. The first spacecraft with this purpose was Clementine. It was launched in 1994 and it was equipped with the Ultraviolet/Visible (UV/Vis) and the Near-Infrared CCD (NIR) cameras (Nozete, 1995), which combined 11 filters between 300 nm and 2700 nm. This spectral range was selected to obtain information suitable for the recognition of the dominant minerals on the surface of the Moon (**Figure 1**). Clementine was followed by the Lunar Prospector, launched in 1998, it allowed the derivation of potassium, thorium, and iron maps of the surface from its gamma-ray spectrometer (Lawrence et al., 1998). The Selenological and Engineering Explorer (SELENE/Kaguya) was launched in 2007 (Sasaki et al. 2003), it was the first hyperspectral sensor orbiting the Moon, its Spectral Profiler consisted of 296 bands between 522 nm and 2600 nm. Shortly after, in 2008, the Chandrayaan-I spacecraft was launched, and its payload included the imaging hyper-spectrometer M^3 (Pieters et al., 2009, Green et al., 2011). M^3 acquired data in the spectral range between 430 nm and 3000 nm, similarly to Kaguya/Spectral Profiler, but with a higher spatial resolution. It operated in two spectral sampling modes: the "Target Mode", characterized by a spectral sampling of 10 nm, with a total of 256 channels; and the "Global Mode", reaching a spectral sampling of 20 nm in the shorter wavelengths and 40 nm in longer ones, adding up to 85 channels (Green et al., 2011). In both cases the spatial resolution is around 110 meters/pixel, and the spectral cubes usually cover long swaths. Due to the limited amount of the targeted mode products and the almost total coverage of the global mode ones, we decided to optimize the workflow for the latter.

1.1 Lunar mineralogical diversity

Following lunar mineralogy, the hyperspectral remote sensing instruments around the Moon acquire data in the spectral interval between 0.45 μm and 3 μm, corresponding to the range where the major mafic minerals exhibit clear absorption features. **Figure 1** shows an example of some minerals with scientific interest on the Moon (pyroxene, plagioclase, and olivine) showing specific spectral signatures in the visible-near infrared range (Arnold et al., 2016). Olivine presents three absorption features ranging between 0.85 μm and 1.3 μm, this is attributable to the presence of Fe2+ within the M1 and M2 octahedra sites (e.g. Burns 1993), creating a wide absorption feature around 1.1 μm. Nevertheless, changes in the composition of the olivine can slightly shift the position of the band center of the absorption, with a shift towards longer wavelengths with increasing fayalite, i.e. Fe^{2+} (e.g. Burns, 1993; Sunshine and Pieters, 1998). Pyroxene exhibits two strong absorptions located at 1 μm and 2 μm, respectively. These absorptions are mainly the result of crystal field transitions of Fe^{2+} cations in the M1 and M2 octahedral sites, whoever, the presence of different abundance of Ca^{2+} (and related Mg^{2+}) also influence the absorption bands of pyroxenes (Burns, 1993; Klima et al. 2011). In fact, pyroxene with a larger amount of Fe^{2+} and Ca^{2+} show band center positions shifted towards longer wavelengths (Klima et al., 2007, 2011) as well as extreme composition shows wider 1.0 μm and weak or absent 2.0 μm band. Different from the other major minerals, plagioclase has a higher

reflectance and its almost featureless in the near-infrared (NIR), even if small amount of Fe^{2+} produce an absorption band around 1.3 μm, which is not easily recognizable in the data of M^3 (e.g. Ohtake et al., 2009, Cheek et al., 2013, Serventi, 2013). To properly analyze the plagioclase composition, one should rely on thermal infrared (TIR) data, such as the one obtained by the Diviner instrument onboard the Lunar Reconnaissance Orbiter (LRO)(Lucey et al., 2021), or the Spectral Profiler onboard SELENE/Kaguya (Lemellin, 2019). An additional shallow absorption band centered around 3 μm, which is associated to hydrated minerals, has been identified by M3 data (Pieters et al., 2009). As well as an absorption feature between 1.5 μm and 3 μm, related to the presence of spinels (Pieters et al., 2014, Moriarty et al., 2023). In general, a spectrum that shows an absorption feature at 2 μm indicates the presence of pyroxene, one with a stronger signal at 1 μm implies the presence of olivine, and a spectrum with shallow absorption in both regions represents an absence of the mafic minerals, and thus the abundance of plagioclase.

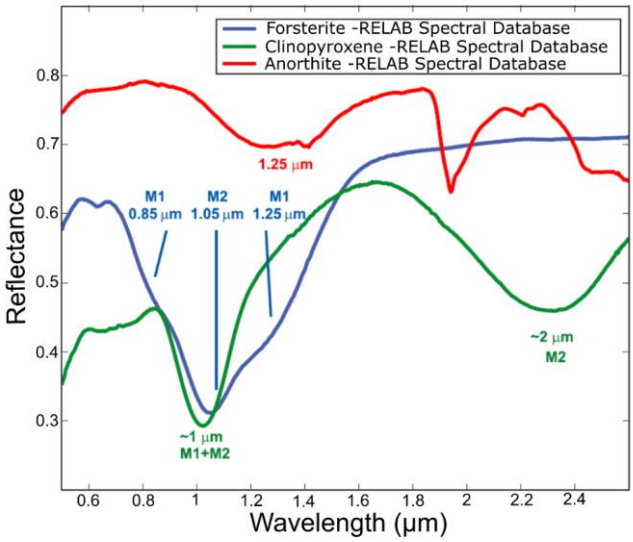

Figure 1: Spectral signatures of the main mineral species on the lunar surface. The three absorption features of olivine are shown in blue (M1, M2, M3). The two absorptions of pyroxene are shown in green (M1, M2). The high reflectance spectrum of plagioclase is shown in red, showing the occasional absorption feature at 1.3 μm. Modified from Arnold et al. (2016).

Since the lunar surface is a mixture of minerals, the actual spectrum is more complex than the ones obtained from single species (**Figure 2a)**. Other factors also add a layer of complexity. Instrumental errors need to be considered, as well as the overall signature of the regolith (Green et al., 2011). But the bigger factor is that the lunar spectra show an overall positive and steep slope (**Figure 2a**), this effect is known as spectral reddening and is the result of space weathering. This alteration is produced by the combined action of solar wind, cosmic radiation, and micrometeoroids bombardment; which produces nanophase iron particles, responsible for the increased spectral slope, a reduction of the reflectance, and the weakening of some absorption bands (Hapke, 2001; Xu et al., 2023). Spectral reddening hinders the absorption

band analysis; therefore, it is necessary to remove the spectral slope. A typical way to remove the spectral slope effects is to apply a continuum removal (**Figure 2b**).

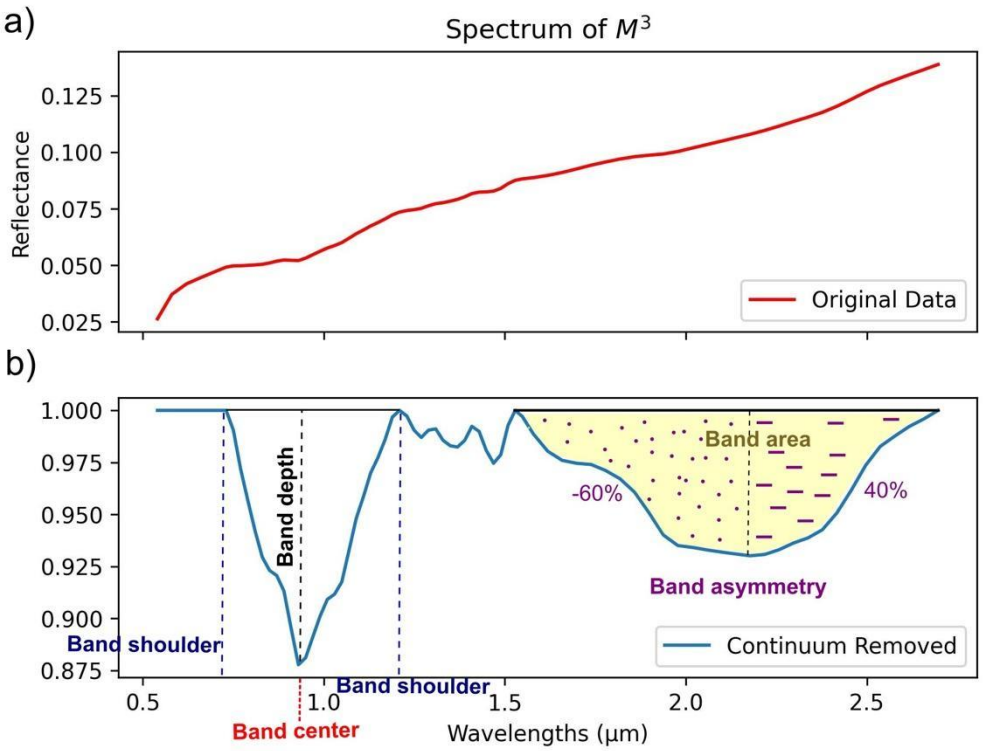

Figure 2: a) Example of a reflectance spectrum of M^3 before continuum removal, showing the steep slope of the continuum. b) Same spectrum after the continuum removal. The main spectral parameters are indicated in the plot. The band center is the wavelength at the minimum point of the absorption, the band depth is the value at the minimum, the band shoulders limit the absorption, the band area is the total coverage of the absorption, and the asymmetry measures the distribution of the area at each side of the minimum as a percentage.

1.3 Techniques to use spectral data

Several approaches can be used to analyze spectral data acquired by remote sensing instruments. The most common method is the use of spectral indexes, those are specific combinations of bands, or band operations, that highlights a specific portion of the spectrum and thus a mineralogical composition (e.g. Montero et al., 2023). The definition of the indexes is supported by an analysis of the spectral parameters of the identified absorption bands (band centers, depth, shoulders, areas, spectral slopes, etc) (**Figure 2b**); or by operating over several bands, like calculating spectral ratios. In some cases indexes are presented as RGB composites, false-colored images that are created by combining three indexes in the red, green, and blue

channels. This allows an easier visualization of the results by comparing several indexes at the same time and supporting the interpretation (Liu and Mason, 2009).

Other techniques can be applied to spectral datasets. Spectral unmixing model are also applied in image analysis (Horgan et al., 2022), and other ones allows the retrieval of mineralogical information from a representative spectrum Modified Gaussian Model (MGM) (Sunshine et al., 1990; Clenet, 2009) or the radiative transfer models (Corley et al., 2018). These techniques focus on the reconstruction of synthetic spectrums using the Hapke reflectance model (Hapke, 1993), which computes the expected reflectance of minerals from their chemical and crystallographic properties. Although the spectral indexes technique does not easily allow an absolute measurement of mineral abundances in complex surface spectrums, it is the most flexible, as the types of indexes that can be created are endless. This allows a targeted survey of desired minerals and an easy analysis of their spatial relationships with other ones, including minor species like spinel and water ice. For the previous reasons, we focused our work on the compilation of spectral indexes present in the literature for the Moon and within the spectral range of M^3, to later recreate them on the Open-Source programming language Python.

1.2 Original formulations that are being replicated

The spectral parameters are intrinsic to the mineral species, which means spectra are comparable regardless of the planetary body. Many parameters were defined in the laboratory (e.g. Adams and Filice, 1967; Adams, 1974; Karr, 1975), and were later applied to the Moon. A detailed list of all the spectral indexes considered in this work is shown in **Table 1**. Spectral indices depend on the characteristics of the spectra considered, for this reason, literature provides a large and evolving number of parameters. Therefore, no unified database of spectral indexes for the Moon is present. Nevertheless, some works went a long way listing important indexes. Zambon et al. (2020) describes eleven indexes suitable for being derived from the data of M^3. These indexes focus on the band centers and band depths around 1 μm and 2 μm, which help on the identification of mafic minerals; the spectral slope, which is a way to measure the maturity of the surface; and a Clementine-like color composite map (Red: 750 nm/540 nm, Green: 750 nm/1000 nm, Blue:540 nm/750 nm), worthwhile to identify regions enriched in mafic minerals (with different enrichment on iron or titanium), plagioclase and glass-bearing materials (Lucey et al., 2000).

The rest of the collected indexes were thought of for specific cases. Wu et al. (2012) updated the FeO and TiO parameters formulated by Lucey et al. (2000). Horgan et al. (2014) used the band area and asymmetry to highlight different mineral and glass compositions. Corley et al. (2018) defined a simple band ratio to highlight the presence of olivine, and Bretzfelder et al. (2020) made an RGB composite based on the integrated band depth (IBD) around 1 μm and 2 μm, and the band depth at 1.9 μm to create a contrast between olivine and the two types of pyroxenes. Besse et al. (2011) also used the integrated band depth (IBD) to differentiate between pulses of lava floods. Finally, Pieters et al. (2014) and Moriarty et al. (2023) used band ratios of non-continuum removed spectrums designed to detect spinel and anorthosite. Finally, we adapted three other indexes for this work, the band area and asymmetry at 2 μm, and a chromite parameter following the formulation of Moriarty et al, 2023.

184

Parameter Name	Abrev. Name	Formulation	Interpretation	Source
Reflectance at 540 nm	R540	$R540$	High values → bright fresh material, plagioclase. Low values → dark terrain, pyroxene.	Adams and McCord (1971)
Band center at 1 µm	BCI	$BCI = \min \sim \left(\frac{R1000nm}{R_c 1000nm}\right)$ $R_C = Removed\ continnum\ spectrum$	Compositional variations of the principal mineralogical phases (pyroxenes, olivines, and plagioclases). If the band depth is shifted to lower wavelengths, it may show abundance of low-Ca pyroxene.	Adams (1974)
Band center at 2 µm	BCII	$BCII = \min \sim \left(\frac{R2000nm}{R_c 2000nm}\right)$	If the band center is shifted to lower wavelengths, it may show abundance of low-Ca pyroxene.	Adams (1974)
Band depth at 1 µm	BDI	$BD1000 = 1 - \frac{R1000nm}{R_c 1000nm}$	Abundance of the principal mineralogical phases and their grain sizes, also abundance of opaque phases.	Adams (1974)
Band depth at 2 µm	BDII	$BD2000 = 1 - \frac{R2000nm}{R_c 2000nm}$	Abundance of the principal mineralogical phases and their grain sizes, also abundance of opaque phases.	Adams (1974)
Spectral slope at 1 µm	SS	$Sl = \frac{R(Max\ shoulder\ BCI) - R540nm}{(Wave(Max\ shoulder\ BCI) - 540nm) * R540nm}$	Low values → fresh terrains, dark terrain. High values → older terrains, space weathering.	Hazen et al. (1978)
Clementine -like red channel	Clem RED	$Clem\text{RED} = \frac{R750nm}{R540nm}$	High values imply low titanium regions, or high glass contents.	Lucey et al. (2000)
Clementine -like green channel	Clem GREEN	$Clem\text{GREEN} = \frac{R750nm}{R1000nm}$	High values show enrichment of iron in the surface, and mafic minerals.	Lucey et al. (2000)
Clementine -like blue channel	Clem BLUE	$Clem\text{BLUE} = \frac{R540nm}{R750nm}$	Higher values imply high titanium content and bright slopes.	Lucey et al. (2000)

Band depth at 1.9 µm	BD1900	$BD1900 = 1 - \frac{R1900nm}{R_c1900nm}$	Highlights differences in mafic compositions when combined with IBDI and IBDII.	Bretzfelder et al. (2020)
Integrated band depth at 1 µm	IBDI	$IBDI = \sum_{n=0}^{26} 1 - \frac{R(789nm + 20n)}{R_C(789nm + 20n)}$	It shows high values when olivine and pyroxene are present.	Bretzfelder et al. (2020)
Integrated band depth at 2 µm	IBDII	$IBDII = \sum_{n=0}^{21} 1 - \frac{R(1658nm + 40n)}{R_C(1658nm + 40n)}$	It shows high values when pyroxene is present.	Bretzfelder et al. (2020)
Band area at 1 µm	BAI	Total area of the absorption feature at 1 µm, this is computed as the summatory of one minus the value of each channel multiplied by the spectral resolution, between the left and right shoulders of the absorption. This is done after the continuum removal.	Useful to differentiate between mineral species.	Cloutis et al. (1986)
Band area at 2 µm	BAII	Total area of the absorption feature at 2 µm, this is computed as the summatory of one minus the value of each channel multiplied by the spectral resolution, between the left and right shoulders of the absorption. This is done after the continuum removal. Closed at 2.5 µm.	Useful to differentiate between mineral species.	This paper
Band asymmetry at 1 µm	ASYI	Difference in percentage between the right and left sides areas of the absorption at 1 µm. A negative value is an asymmetry to the left, a positive one to the right.	Useful to identify glass-bearing mixtures with high asymmetries.	Cloutis et al. (1986)
Band asymmetry at 2 µm	ASYII	Difference in percentage between the right and left sides areas of the absorption at 2 µm. A negative value is an asymmetry to the left, a positive one to the right. Closed at 2.5 µm.	Useful to identify glass-bearing mixtures with high asymmetries.	This paper
Olivine parameter	Ol	$Ol = \left(\frac{R1699}{0.1 * R1050 + 0.1 * R1210 + 0.4 * R1329 + 0.4 + r1469}\right) - 1$	A higher value implies a major abundance of olivine.	Corley et al. (2018)
Spinel ratio	Sp1	$Sp1 = \frac{R1450nm}{R1750nm}$	A higher value implies a major abundance of spinel.	Pieters et al. (2014)

Spinel ratio	Sp2	$Sp2 = \frac{\left(\frac{R1250nm - R750nm}{500}\right) * 1350 + R1250\ nm}{R2600nm}$	A higher value implies a major abundance of spinel.	Moriarty III et al. (2022)
Pyroxene ratio	Px	$Px = \frac{R700nm + R1200nm}{R950nm}$	A higher value implies a major abundance of pyroxene.	Pieters et al. (2014)
Pure anorthosite ratio	An	$Px = \frac{R1000nm + R1500nm}{R1250nm}$	A higher value implies a major abundance of anorthosite.	Pieters et al. (2014)
Band depth at 950 nm	BD950	$BD950 = 1 - \frac{R950nm}{R_c 950nm}$	Combined in RGB6 is useful to study lunar maria.	Besse et al. (2011)
Badn depth at 1.05 µm	BD1050	$BD1050 = 1 - \frac{R950nm}{R_c 950nm}$	Combined in RGB6 is useful to study lunar maria.	Besse et al. (2011)
Badn depth at 1.25 µm	BD1250	$BD1250 = 1 - \frac{R1250nm}{R_c 1250nm}$	Combined in RGB6 is useful to study lunar maria.	Besse et al. (2011)
Reflectnace at 1.58 µm	R1580	$R1580nm$	Combined in RGB7 is useful to study lunar maria.	Besse et al. (2011)
Iron oxide parameter	Fe	$Fe = -\ arctan\ arctan\left(\frac{\left(\frac{R918nm}{R757nm}\right) - 1.19}{R757nm - 0.06}\right)$	Higher values imply the presence of iron.	Wu et al. (2012)
Titanium parameter	Ti	$Ti = arctan\ arctan\left(\frac{\left(\frac{R561nm}{R757nm}\right) - 0.71}{R757nm - 0.07}\right)$	Higher values imply the presence of titanium.	Wu et al. (2012)
Chromite parameter	Cr	$Cr = \frac{\left(\frac{R1350 - R750}{600}\right) * 1500 + R1350}{R2750}$	Higher values imply the presence of chromite.	This paper

RGB composite	Abrev. Name	Formulation	Interpretation	Source
RGB Clementine -like color composite	Clem	R: ClemRED, G: ClemGREEN, B: ClemBLUE.	Red channel → low titanium regions, or high in glass content (see the highlands, pyroclastic deposits). Green channel → amount of iron in the surface, mafic minerals. Blue channel → high titanium. Lunar surface maturity.	Lucey et al. (2000)
Color composite 1	RGB 1	R: SS, G: BDI, B: BDII.	When red dominates, space weathering is major, blue/green zones correspond to less mature terrains.	Zambon et al. (2020)
Color composite 2	RGB 2	R: SS, G: R540, B: BCII.	Blue areas are characterized by high iron/titanium, red zones are a lack of that.	Zambon et al. (2020)
Color composite 3	RGB 3	R: SS, G: R540, B: BDI.	This RGB combination gives information on terrain maturity and reflectance.	Zambon et al. (2020)
Color composite 4	RGB4	R: BCI, G: BCII, B: BAI.	Pyroxene rich material is seen in blue/yellow/green, glass and olivine in pink/yellow, plagioclase in red.	Horgan et al. (2014)
Color cmposite 5	RGB5	R: ASYI, G: BCII, B: BAI.	Pink and yellow show glass-bearing mixtures.	Horgan et al. (2014)
Color composite 6	RGB6	R: BD950, G: BD1050, B: BD1250.	Blue means presence of olivine, red/purple pyroxene.	Besse et al. (2011)
Color composite 7	RGB7	R: IBDI, G:IBDII, B: R1580.	Red is olivine rich.	Besse et al. (2011)
Color composite 8	RGB 8	R: BD1900, G: IBDII, B:IBDI.	Dark blue corresponds to olivine signatures, cyan to clinopyroxene.	Bretzfelder et al. (2020)
Spinel	Spanpx	R :Px, G: Sp2, B: An.	Amount of spinel.	Moriarty III et al. (2022)

Table 1: List of spectral indexes collected in literature. A total of 28 parameters and 10 RGB composites were implemented.

2. Data

As our goal was to generate a set of consistent spectral indexes, we opted for optimizing the tool for the global mode captures of M^3, in this way we always worked with the same spectral sampling and similar spatial resolutions. We selected the data from the Planetary Data System (PDS) (Malaret et al., 2011), using the PDS Geosciences Node Lunar Orbital Data Explorer (LODE) search tool.

2.1 Data formats

M3 data is available as cubes in IMG format, each cube is a three-dimensional array of data, which stores spatial information in a two-dimensional plane, and spectral information in depth. Other additional files contain ephemerides, pointings and geometries, calibration data, and metadata. To map-project the cubes it is necessary to download both the calibrated radiance and the derived reflectance images, although only the latter is used for the retrieval of spectral parameters. The reflectance cubes available in the PDS have 83 bands, missing the first two bands, corresponding to 0.46 μm and 0.5 μm. The reflectance data is already calibrated for thermal and photometrical anomalies (Lundeen et al., 2011). The spatial resolution of the global mode data is around 110 meters/pixel, while the spectral sampling is variable, being 0.02 μm between 0.5 μm to 1.5 μm, and 0.04 μm between 1.5 μm and 3 μm. Global mode cubes cover a substantial portion of the lunar surface, so one or two cubes are usually enough to study medium-sized geoforms on the lunar surface. On the global mode, the data is captured at full resolution, afterwards, it is averaged to reduce it to the desired value. M3 captured data intermittently across two orbital periods, usually with high solar zenith angles (Green et al. 2011). As a result, there are not many locations covered by more than one or two cubes taken at different times.

M3 data is affected by some artifacts, making it difficult to develop general procedures to remove or improve these issues. In particular, all M3 files display vertical stripes due to thermal issues with the instrument. The stripes are present in all wavelengths, but their intensity varies from cube to cube. We also detected an anomalous increase in reflectance from right to left in some cubes. This effect is particularly strong at longer wavelengths, affecting the band depth, area, and asymmetry (Green et al., 2011). The photometric correction of the cubes is not reliable for incidence angles higher than 70 degrees, which especially affect steep slopes on craters. Finally, there are some cubes taken in the same area that are not correctly projected with respect to each other, this may be a problem with the SPICE information of the data (Acton et al., 2016). Although the prior artifacts reduce the quality of the information, almost every cube still has plenty of data that can be analyzed.

2.2 Case study regions

All the indexes collected and formulated in this work are applicable to any location on the lunar surface, but here as case of study, we compare our results with those of other three authors that also focused on spectral indexes (**Figure 3**).

2.2.1 Apollo Basin

The Apollo basin (36.1°S 151.8°W) was the target of Zambon et al. (2020). It is a large multiring impact basin within the northern part of the South Pole Aitken basin (SPA) (Moriarty and Pieters, 2018). It has an estimated age of 3.98 Ga (Ivanov et al., 2018) and was later fulfilled

by basaltic flood lavas. The Apollo basin has a big geomorphological and compositional diversity (Ivanov et al., 2018, Potter et al., 2018), most of the zone is dominated by highlands terrains, but a large basaltic flood is emplaced at the center of the basin. This diversity makes it a good target to test the spectral parameters variability. Zambon et al. (2020) used the band center, depth, and spectral slope to study the mineralogical composition of the region, we will compare our results for these same parameters. We used the reflectance cube M3G20090813T213525.

2.2.2 Vallis Alpes

Vallis Alpes (49°N, 3°E.) was studied by Bretzfelder et al. (2020). The Vallis Alpes and Montes Alpes are landforms located in the northern rim of the Imbrium basin, they are northeast trending structures, including a central linear rille and parallel mountain ranges at both sides of it. The mountains are probably ejecta blocks of the Imbrium impact, which according to Klima et al. (2011) are enriched in low-Ca pyroxene. Bretzfelder et al. (2020) identified olivine outcrops in the surface using the integrated band depths and the band depth at 1.9 μm, suggesting the presence of plutonic rocks excavated from the lower crust (Shearer et al. 2015). We recreated these parameters to identify the presence of olivine in the region. The reflectance M^3 image used for this target is named M3G20090608T125102.

2.2.3 Aristarchus crater

The Aristarchus Crater (23.4°N, 47.2°W) was analyzed by Horgan et al. (2014). It is a well-preserved Copernican complex crater, it shows high albedo and sharp morphologies, which correspond to impact products (Mustard et al., 2011). The structure of its ejecta is clearly visible, including several types of impact melt, basement rocks and structural patterns. Horgan et al. (2014) used the band centers, areas and asymmetries to study and classify the ejecta and glass bearing lithologies around the crater. The reflectance M^3 cube used for this target is named M3G20090209T054031.

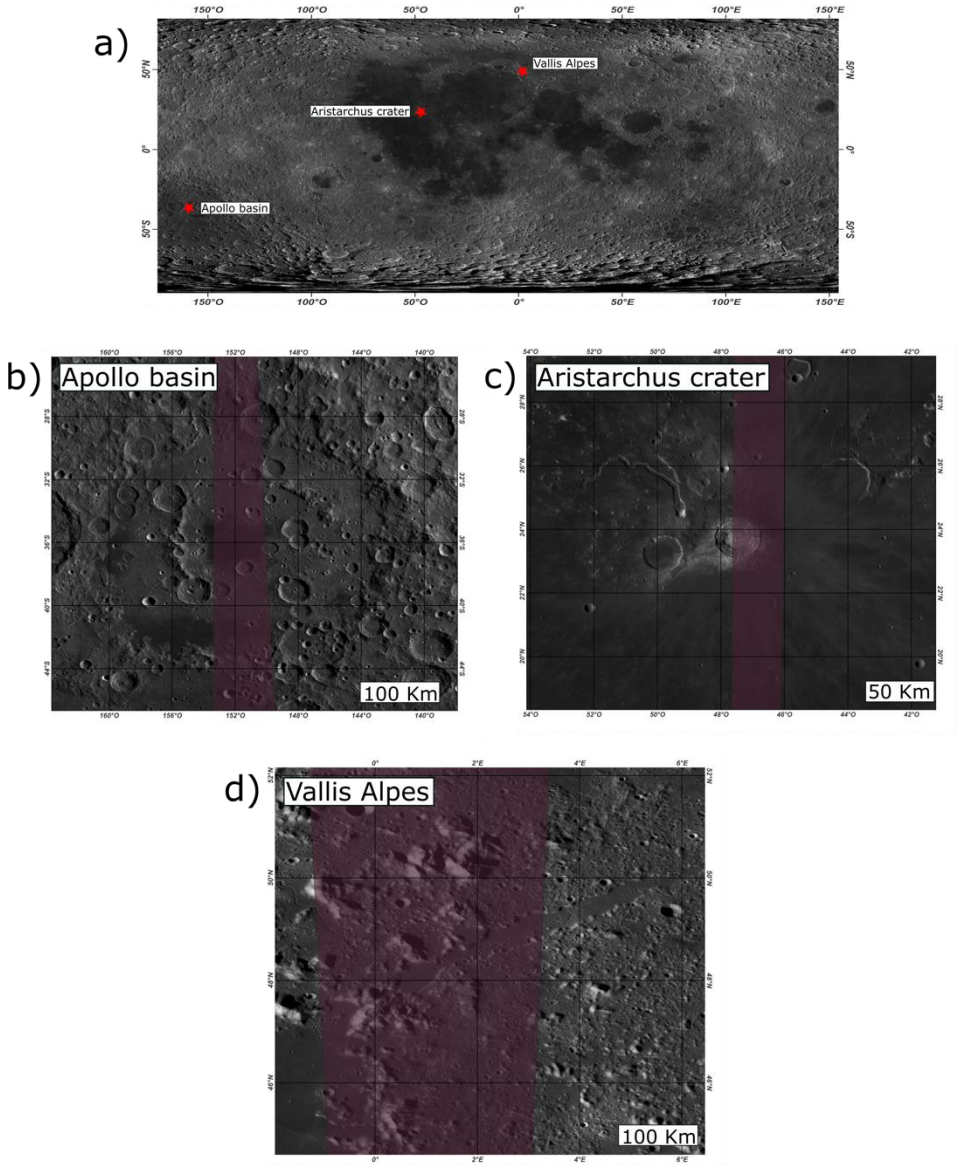

Figure 3: a) Regions selected to test the MoonIndex tool. b) Apollo Basin, a large impact structure in the South Polar Aitken basin (SPA), target of Zambon et al. (2020). c) Aristarchus crater, a Copernican impact structure enriched in glasses, target of Horgan et al. (2014). d) Vallis Alpes, a linear rille in the rim of the Imbrium basin, target of Bretzfelder et al. (2020).

3 Methods

The use of other software is necessary before and after the application of ***MoonIndex***. An important step to properly use remote sensing images is the spatial projection of the data, which locates the images on the surface of a planet. For planetary bodies, this process is challenging, and has been optimized before in software like the Integrated Software for Imagers and Spectrometers (ISIS) (Laura et al., 2023). For this reason, we did not recreate this step within the Python workflow. Then, MoonIndex can be applied to map-projected M^3 reflectance cubes. As

for the indexes derived from our tool, we strongly recommend their use with geospatial software such as QGIS or ArcGIS, which are well-optimized for high level remote sensing data interpretation. The whole workflow applied is summarized in **Figure 4**.

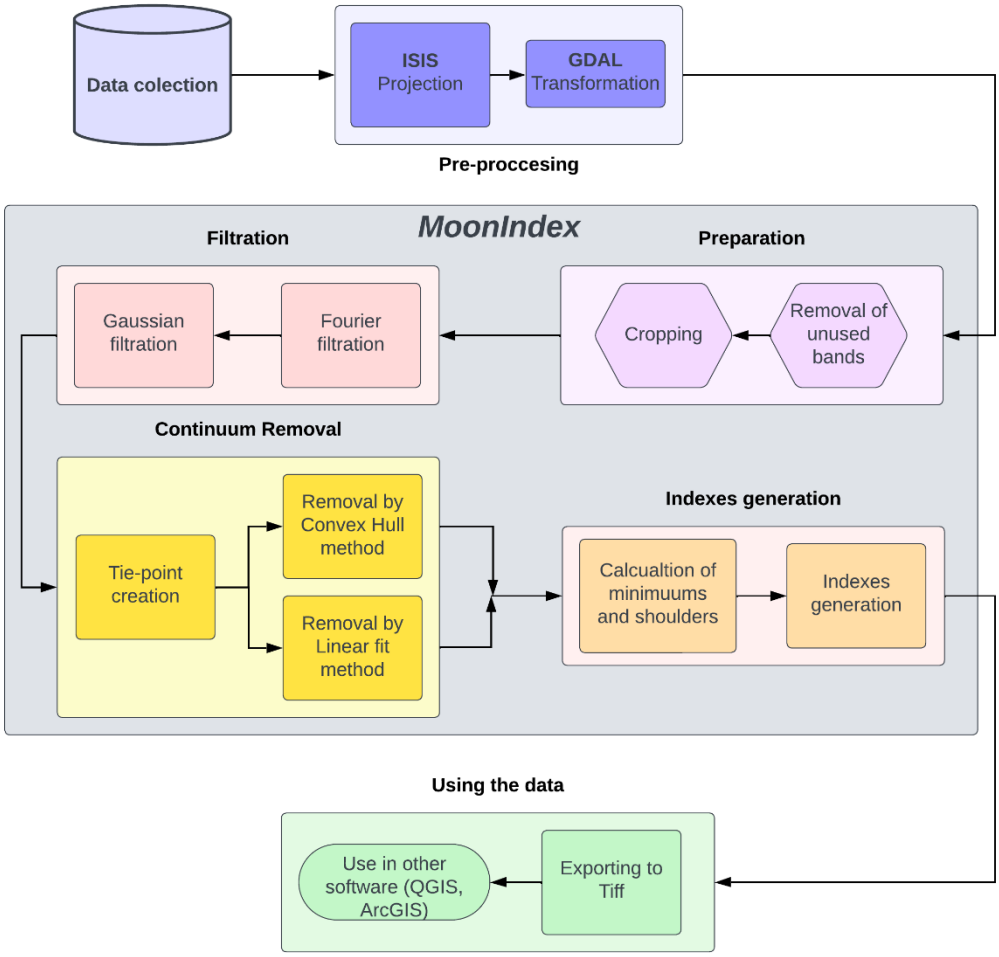

Figure 4: Flow-chart of the full procedure to create spectral indexes using *MoonIndex*.

3.1 Preprocessing

To use M^3 cubes in Python, one first need to map-project them and change their format to Tiff/Geotiff using ISIS and the Geospatial Data Abstraction Library (GDAL) (Rouault et al., 2023).The first step is the ingestion of the data to ISIS, the importing command of ISIS only accepts the radiance product of M^3, so we did – essentially a workaround - a change in the associated LBL file of the radiance cube to use the reflectance data (e.g., Figuera et al., 2018). The modification consists in changing the name of the radiance cube by the one of the reflectance cube in the "^RDN_IMAGE" parameter under the "/* Spectral calibration parameters and radiometric gain factor data */" section of the LBL file. This tricks ISIS to accept the reflectance cube, and to continue the pre-processing. As the data of M^3 usually covers substantial

portion of the Moon, sometimes it is necessary to reduce the extent of the cube, this is usually necessary when the data comprises the poles. The polar region covered by the cube can be cropped to a smaller size in ISIS. Then, we geographically projected the cube to a pre-defined coordinate system. After the projection, the format of the data was changed from CUB to TIF using GDAL. At this point, the data is ready to be ingested on the tool. The commands used in this step ca be found in **Text S1**.

3.2 Data processing using Python

The ***MoonIndex*** tool is designed to automatically work, after an initial configuration of the input and output paths. The indexes are calculated from a set of Python functions developed in this work, which are optimized for the technical characteristics of M^3. The workflow can be divided into three main stages (**Figure 4**): filtration, continuum removal (when needed), and indexes generation. We used Python libraries that are produced/written to work with spatial imagery data, like *xarray* (Hoyer and Joseph, 2017), *openCV* (Bradsky, 2000), and *rasterio* (Gillies and others, 2013). As well as common operational libraries like *numpy* (Harris et al., 2020), and plotting ones like *matplotlib* (Hunter, 2007). A detailed description of the libraries is found in **Text S2**.

3.2.1 Cube adjustments

Some minor corrections are needed before working with the data. The first two bands of the reflectance cube do not contain spectral information, so they are removed, this means that the initial band of the data is 0.54 μm. As the cubes are projected, they no longer have a rectangular shape, so pixels with no data values appear at the edges, all of them are reassigned to zero, to avoid problems in the processing. Due to the M3 observation strategy, a large part of the cubes is acquired from north to south pole, increasing the file dimension and making the data processing difficult (Green et al., 2011). For this reason, a specific tool to resize the data is fundamental for easier data processing. In this regard, we develop a function dedicated to slicing the data using

the coordinates of the desired regions (**Figure 5**). Nevertheless, the user can still opt to process the full cube by simply not using this function.

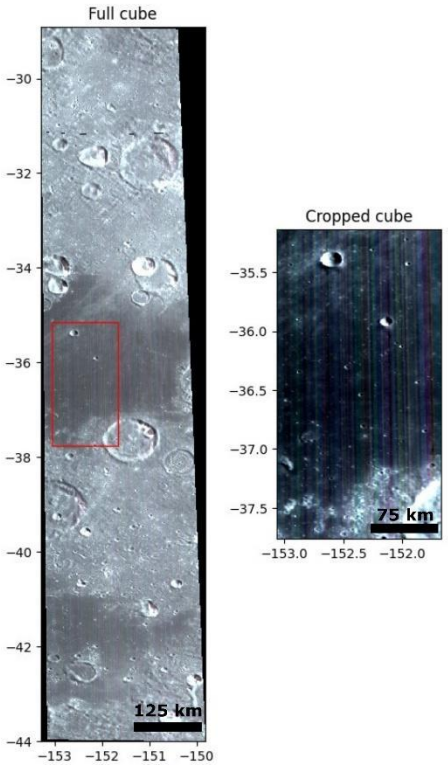

Figure 5: Cropping function of the tool. M3 cubes are generally large, so the use of subsections when possible is recommended.

3.2.2 Filtration

The striping of the cubes can disrupt the data, both the spectral profiles and the images for each wavelength have a periodic noise that makes interpretation more difficult (**Figure 6a**). Since no instrumental calibration is provided by the team of M^3, we opted for image and data filtration. We followed the two filtration steps proposed by Shkuratov et al. (2019), which consists of a Gaussian convolution followed by a Fourier filtration, nevertheless, after several attempts we obtained better results inverting the order of the filters, as less stripping is visible after generating the indexes.

The Fourier filtration was computed individually for each band of the cube. The process starts by applying a 2D Fourier transform, the resulting image is in the Fourier or frequency domain, which shows the distribution of frequencies contained in the original spatial domain (Broughton & Bryan, 2018). In the Fourier domain, it is possible to identify some frequencies responsible for the vertical striping of the data, which cross horizontally the Fourier image at its center (**Figure 6b**). Once the position of the stripes was identified, we applied a mask to the data, multiplying by zero the regions dominated by their frequencies (**Figure 6c**). The size of the mask corresponds to 60% of the width of the image, and 2% of its altitude; these measurements were

established manually as it removes the major number of stripes without damaging the frequencies of the actual data, usually accumulated at the center of the Fourier image. The user has the possibility to change the size of the filter. Lastly, an inverse Fourier transform is applied to the masked images, recovering the filtered cube in the spatial domain. After the Fourier filtration, a simple 1D Gaussian filter is applied to the data, this time in the spectral dimension. This process smooths the spectral signatures of each pixel, allowing the identification of the main mineral absorption bands (**Figure 7a**). The filter is only applied between 0.54 μm and 2.85 μm, to avoid an undesired trend caused by the instrumental errors at the longer wavelengths captured by M^3. As most of the minerals on the Moon have absorption bands in shorter wavelengths, we decided not to include those unfiltered last four bands. Finally, we examined that the filters do not affect the actual data. We generated images ratio between the filtered and unfiltered cubes, and then checked that, variations of over 2% were not made outside the vertical stripes (**Figure 7b**).

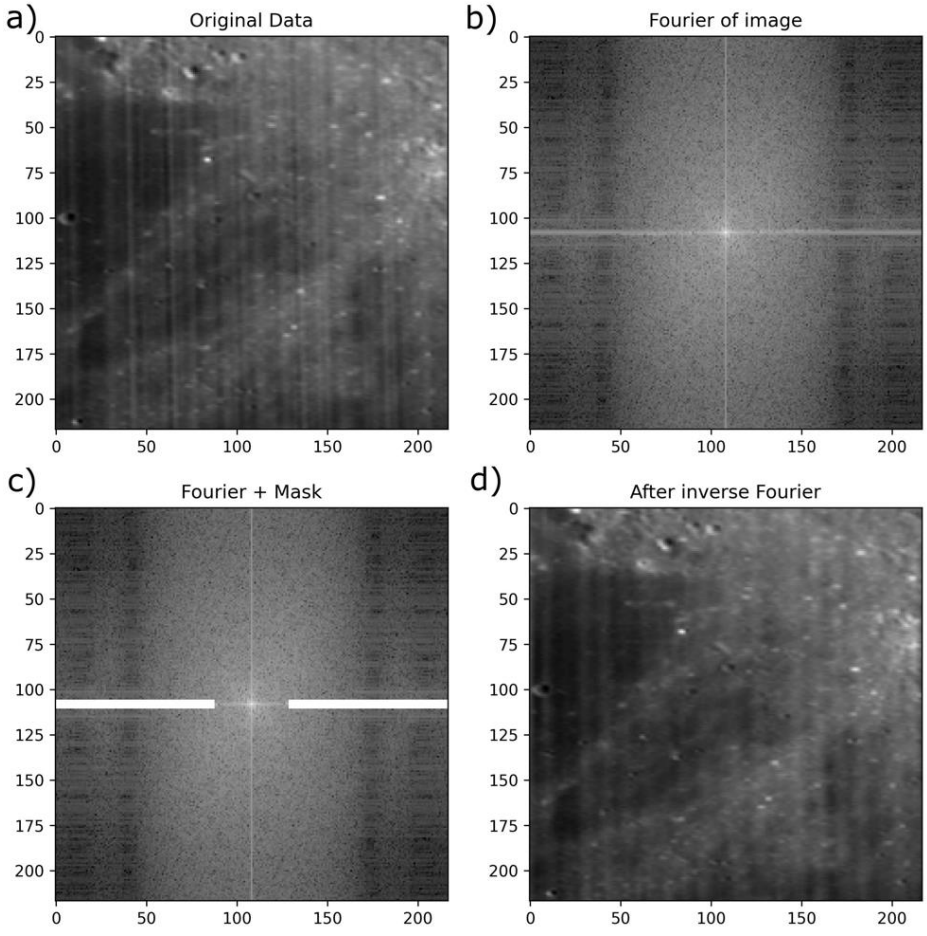

Figure 6: Fourier filtration of the cube. a) Original data with the typical vertical striping of M^3.b) Fourier image of the data, the strong horizontal line contains the frequencies of the

vertical stripes. c) Filter applied to the data, the pixels inside the rectangles are multiplied by zero. d) Image after the filtering, showing reduced vertical stripes.

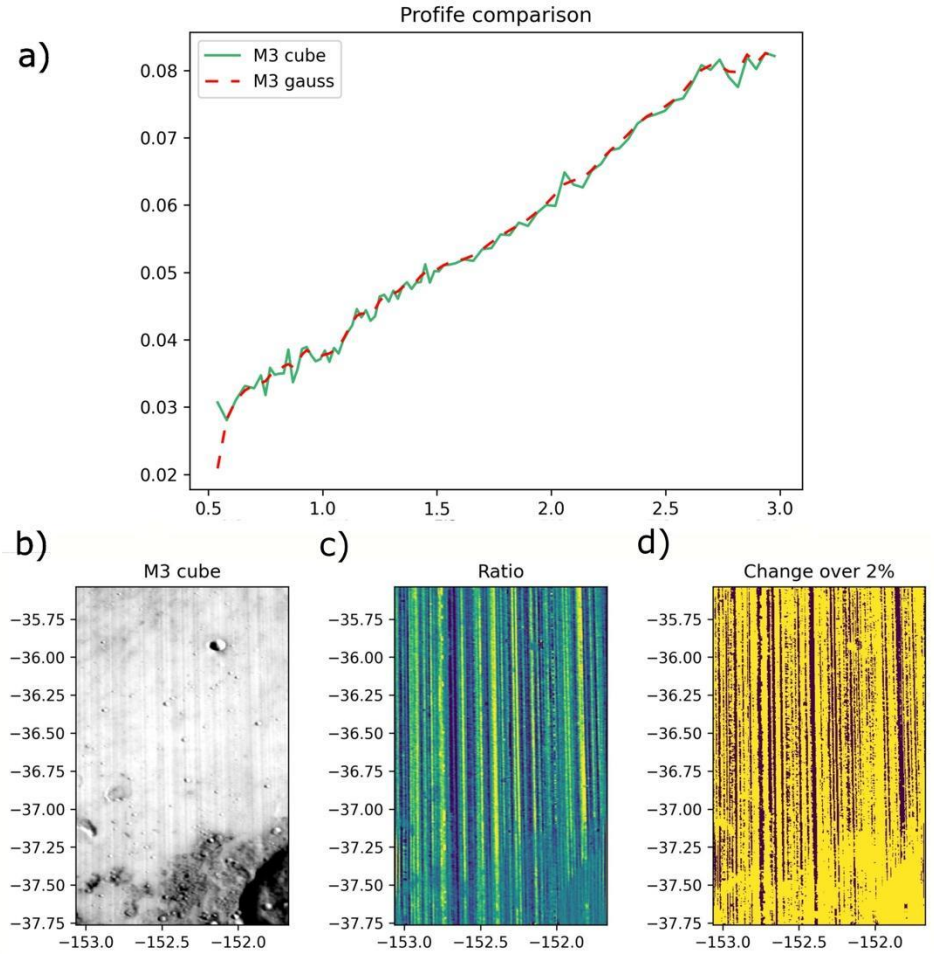

Figure 7: a) Comparison of the spectral profiles before and after the Gaussian filter, the orange line is smoother and allows a better interpretation of the absorption bands. b) Images of the original cube, c) the ratio between the last and the Gaussian-filtered cube, d) and the location with changes over 2% on reflectance (black pixels). These images show the surface data is not affected by the filtering process.

3.2.3. Continuum removal

Some indexes require the continuum removal to be performed. The continuum of a spectrum is considered the background absorption signal, which results from the interaction of several properties of the analyzed surface (e.g., Clark and Rush, 1984; Zhang et al., 2016). The continuum on the spectral signatures of M3 is a positive slope that overlaps the relatively weak absorption of the minerals, it results from the combined signals of the lunar regolith and the products of space weathering. In the lunar case, a major contribution to the continuum is due to the space weathering effects, which in turn can be used to measure the maturity of the surface (Lucey et al., 2000). Even when the continuum plays a major role in M^3cubes, its removal

uncovers the spectral properties of the minerals on the surface and allows the analysis of parameters related to absorption bands (**Figure 8**).

Several approaches have been used to remove the continuum of lunar spectrums, we decided to implement two of these methods in ***MoonIndex***. Since this process consist in removing the overall trend of the data, the most common approach on literature involves calculating the continuum as a linear or polynomial fit between the first and last value of the spectrum, and then use it to divide the original data (e.g., McCord et al., 1972; Clark and Roush, 1984). Similarly to Zambon et al. (2020, and references therein), we applied a linear-fit method to remove the continuum of M^3 data. By considering the spectral properties of the minerals on the Moon surface, the removing function was calculated independently for each absorption band. Around the 1 μm band, a second order fit was used, and for the one around the 2 μm, a linear fit function was applied. We named this approach as the "linear-fit method" in our tool **(Figure 8a)**. Nevertheless, the polynomial order of this method can be modified for both absorption bands. The other approach implemented is the convex hull method (Graham, 1972), in this case, the continuum is calculated as the enveloping function of the spectrum data, consisting of lines interpolated over every consecutive point of the spectrum. This method has the advantage of being completely independent of arbitrary limits and that it highlights the shape of every absorption feature. We implemented this approach as the "convex hull method" in our tool **(Figure 8b)**.

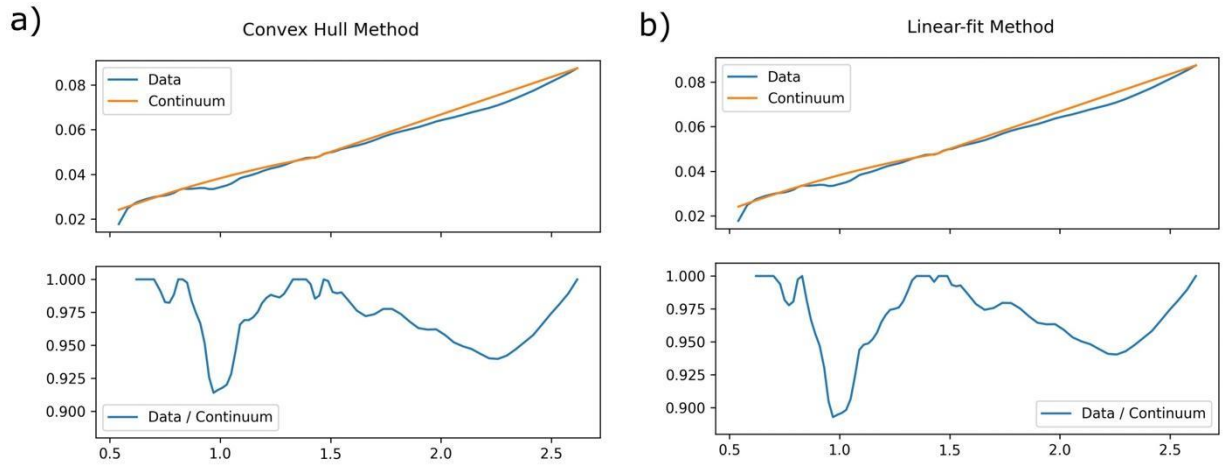

Figure 8: Continuum removal methods applied by *MoonIndex*. a) Convex-hull method, it used an envelope around the vertex of the spectrum. b) Linear-fit method, it used a second order polynomial around the 1 μm absorption band, and a linear fit around the 2 μm absorption band.

An additional challenge was found when the slope of the continuum is exceptionally high, this creates an effect that masks the shoulders of the absorption bands around 1 and 2 μm, resulting in an incorrect calculation of the convex hull and the linear fit. To bypass this problem, we created a break-point between 1 and 2 μm, this point has a higher value than the surrounding data, ensuring that the continuum removal process will count it as a maximum. This artificial point marks the closure of the absorption band at 1 μm and the beginning of the one at 2 μm, only when the spectral signature is too featureless to be detected. The position of the tie-point

was defined as the most prominent peak of the difference between the original spectrum and its continuum, calculated with a linear fit between 1.02 μm and 2.09 μm. We selected this range since the absorption band at 1 μm usually closes inside it.

3.2.4 Key parameters extraction

Once the continuum has been removed, the data is ready for the retrieval of spectral indexes. Two parameters were calculated first, the position of the minimum reflectance and the position of their two surrounding shoulders, for both the 1 μm and 2 μm bands. These parameters are key to calculate other indexes since they define the limits of the two main regions of mineralogical interest. The minimum is also used to derive the band depth, while the shoulders are necessary to calculate the band areas, which in turn allow the definition of the band asymmetries. The position of the minimum reflectance (or maximum absorption) is simply defined as the wavelength where the spectrum has its lower value, this is calculated independently for the 1 μm and the 2 μm band, being the break-point the limit for both. The positions of the shoulders were defined as the first local maximums to the left and right of the band minimum. Since this operation is done after the removal of the continuum, the shoulders have values equal to one **(Figure 2)**. Since the data after 2.65 μm was cut from all the spectrums, this value is the right shoulder of the 2 μm band for every pixel.

Once the continuum removal is calculated we made a second-order polynomial fit around the minimums and maximums to further reduce the noise of the resulting indexes, this is done within a window from two wavelengths lower up to two wavelengths higher.

3.2.5 Indexes generation

A total of 28 indexes were reconstructed in this work. In **Table 1** we report the calculation of the parameters, their significance, and exemplary RGB composites that use them. We created Python functions that generate a raster for every index listed in **Table 1.**

Among the parameters, the ones done before the removal of the continuum consists of simple operations between bands. Those can be quickly calculated in Python after ingesting and filtering the data. As an example, the pyroxene ratio formulated by Pieters et al. (2014) was calculated as:

$$Px = \frac{R700\,nm + R1200\,nm}{R950\,nm} \quad (1)$$

Where R is the reflectance at that wavelength. A list with all the formulations can be found in **Table 1**. For the parameters done after the continuum removal, the calculation involves operations between the continuum and the spectrum. The band center and the band depth are defined as (Adams 1974):

$$BCI = \left(\frac{RB\,nm}{RB_c\,nm}\right) \quad (2)$$

$$BD = 1 - \frac{RB\,nm}{RB_c\,nm} \quad (3)$$

Where RB is the reflectance of the spectrum, and RBc the value of the continuum. The band area was calculated for the two main absorption bands at 1 μm and 2 μm with (Cloutis, 1986):

$$BA = \sum \quad 1 - \frac{RB\ nm}{RB_C\ nm} * SR \tag{4}$$

Where SR is the spectral sampling of the cube, and the summatory is limited by the positions of the shoulders of the absorption bands. Finally, the asymmetry is calculated as the difference in the area between the right and left half of the absorption band (**Figure 2**). Given as a positive percentage when the asymmetry is higher to the right, and negative when it is higher to the left. A more complex index is the integrated band depth (IBD) (Bretzfelder et al., 2020), that is the sum of the band depths at each point along the full extension of an absorption band. It was calculated as:

$$IBD = \sum \quad 1 - \frac{R(B\ nm + SR)}{RB_C(B\ nm + SR)} \tag{5}$$

A few indexes were adapted in this work from previous authors. Horgan et al. (2014) evaded using the band area and asymmetry at 2 μm since the absorption features of pyroxenes at longer wavelengths is not fully captured by the range of M3. Nevertheless, we believe calculating them is still useful, so we use the same method as their counterparts at 1 μm, closing the spectrum at 2.5 μm to avoid hydroxyl absorptions at 2.8 μm and the instrumental errors of the last channels. At last, we generated a chromite parameter. Since the reflectance spectrum of chromite is like the one of spinel, but with absorptions bands located at slightly longer wavelengths (Cloutis et al., 2004), we followed the approach of Moriarty et al. (2023) for spinel. The parameter is a ratio between an extrapolated value at 1.5 μm, using the slope between 750 μm and 1.3 μm, and the reflectance value at 2.7 μm. Like on the spinel parameter, this should highlight regions where the 2 μm absorption is higher than usual. It is important to consider that the spectrum of both minerals is similar, so a unique parameter that differentiates between them is difficult to achieve.

3.2.6 RGB composition delivered

The parameters can be combined between each other in RGB composites to highlight mineral associations or variations in the composition of the surface. **Table 1** shows examples of RGB composites used by previous authors. Among them are the Clemetine-like composite of Lucey et al. (2000), three composites suitable for the exploration of mafic minerals and evaluate surface maturity by Zambon et al. (2020) (RGB1, RGB2, and RGB3), two composites focused on crater ejecta by Horgan et al. (2014) (RGB4 and RGB5), two composites to detect mafic minerals by Besse et al. (2011) (RGB6 and RGB7), the olivine detection composite of Bretzfelder et al. (2020) (RGB8), and the spinel composite of Moriarty et al. (2022). Furthermore, other combinations of parameters can be done to highlight different compositions or mineral associations. For this reason, we created a python function that combines all the

indexes in a single tiff file, this allows the user to reproduce each one of the listed RGB composites and more in a geoprocessing software like QGIS.

3.3 Deployment

MoonIndex is deployed as a python package with an MIT license. It is reachable from the web repositories PyPI and GitHub. Some exemplifying products will be showcased in the Space Browser of the EXPLORE platform (Nodjoumi et al., 2022). The source code of the tool is fully available at GitHub (Suarez-Valencia, 2023), so the user has the option to modify it to its needs.

4 Results

In this section we will showcase our results obtained with the convex hull continuum-removal method for a selected set of indexes, that we will later compare with the results of previous authors. Nevertheless, the results for all the calculated indexes are reported in the supplementary materials (**Figure S2**). The analysis of the images and the subsequent interpretation of the mineralogy are particular to the selected study zones, so the user must consider the regional properties of their targets when using the products of ***MoonIndex***.

4.1 Filtration

Our first goal was to reduce the noise of the data using a Fourier and a Gaussian filter without losing much scientific information of the general shape of the spectrum and the absorption bands. In **Figure 7c**, the ratio between the original image and the filtered one shows that the residual information is concordant with the stripes on the non-filtered cube (**Figure 7b**), furthermore, the crater in the bottom-left has little residuals, since the stripping was not as strong in this location. Another test was to identify the pixels that overcame a change of over 2% during the filtration (**Figure 7d**), which are shown in black. These pixels are consistent with the original striping, which means that the surface information that was visible before the filtration (yellow) was not affected by the process.

4.2 Band center and depth

The bands centers and depths calculated by ***MoonIndex*** for the Apollo basin are shown in **Figure 9a, 9b, 9c, and 9d**. The band center defines the position of the absorption features to study, which in the case of pyroxenes and olivines is related to their composition (Burns, 1993; Klima et al. 2011). The band depth in turn reflects the amount of that mineral, since a stronger signal indicates a higher abundance within a mixture (Clouts et al., 1986). On the Band center at 1 μm there is a clear difference between the areas corresponding to highlands and maria (**Figure 9a**). The first ones have centering values around 0.93 μm, indicating at least a lack of pyroxenes; while in the mare, the band is centered at longer wavelengths, around 1.04 μm, resulting from the presence of pyroxene on the basaltic lavas (Klima et al., 2011). Furthermore, the variations inside the maria hints to a compositional variation of pyroxenes, since OPX tends to have lower center values than CPX. The band depth at 1 μm also allows the identification of mafic minerals (**Figure 9c**), a higher value implies that a major amount of them are present. The band depth at the center of the basin shows values around 0.13, while in the surrounding highlands it is only around 0.05. The band center at 2 μm inside the maria varies between 2.05 and 2.2 μm, further

pointing to some variations in the composition of pyroxenes. Finally, the band depth at 2 µm shows strong absorption in the maria of around 0.08, further pointing to the presence of pyroxene (**Figure 9c and 9d**). Olivine does not show features in the 2 µm spectral range, so a comparison between both band depths can help identify its presence (see Index RGB 8) (Isaacson et al., 2011).

Some instrumental and acquisition artifacts are also seen. The band depth at 2 µm is especially sensitive to the already mentioned thermal instrumental error that causes a decrease of the values from right to left of the M^3 cubes at longer wavelengths (Green et al., 2011), resulting in the maria regions to the left of the image showing a similar depth as the highlands. Regions with incidence angles higher than 70 show anomalous values on all the indexes, therefore information in those zones is not reliable.

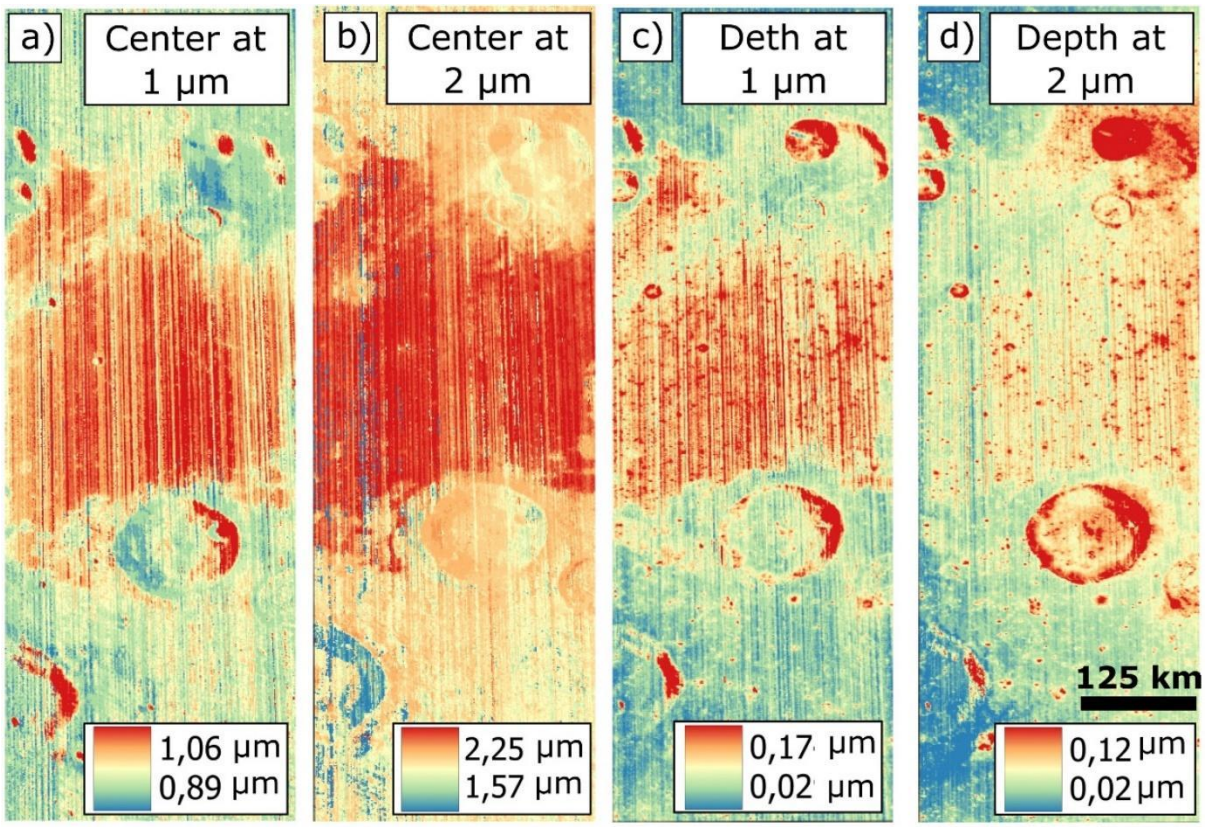

Figure 9: Initial parameters calculated by *MoonIndex* for the Apollo basin. a) Band center at 1 µm, lower values (blue) correspond to highlands materials, while higher values (red) are due to the presence of mafic minerals in the mare. b) Band depth at 2 µm, also allows the differentiation between highlands and mare. c y d) Band center and depth for 2 µm, they serve a similar purpose as their 1 µm counterparts.

4.3 Band area and asymmetry

To showcase the band area and asymmetry obtained by ***MoonIndex***, we use the cubes over the Aristarchus crater, which has a well-preserved ejecta blanket around and a variety of glass-bearing materials (Mustard et al., 2011). The band area corresponds to the region inside the

continuum and the absorption band (**Figure 2**). The band area is useful to identify ejecta (Horgan et al., 2014), as well as mineralogical differences, since OPX-rich ejecta has a higher band area value than CPX-rich ones (Cloutis et al., 1990). The band asymmetry quantifies the shape of the absorption band by comparing the area to the left and right of the band center, negative values imply a bigger area left of the center, and positive values the opposite. The band asymmetry is useful to identify glass and olivine-bearing ejecta, as well as plagioclase. Since mixtures of pyroxene with those materials result in higher asymmetries than only pyroxene (Horgan et al., 2014). For the band area at 1 μm in the Aristarchus crater, the ejecta is clearly recognizable as a zone with low values scattered around the crater (**Figure 10a**). In the band asymmetry at 1 μm, the only contrasting feature is the negative values of the northern ejecta (**Figure 10b)**, which previous authors have identified as a mixture of OPX and anorthosite (Chevrel et al., 2009). In the band area at 2 μm, the pattern of the ejecta is not so clear compared to its 1 μm counterpart, the lower values in the southern half of the ejecta indicate a lower amount of pyroxene on it (**Figure 10c**). As for the band asymmetry at 2 μm (**Figure 10d),** we found that the landforms are clearer than in its 1 μm equivalent. Still, higher values are encountered in the ejecta south of the crater in both asymmetries, pointing to the presence of glass-bearing lithologies (Horgan et al., 2014).

Negative values dominate the 2 μm asymmetry, meaning that the absorption band is broader left of the 2 μm center. This effect is introduced by closing the absorption band at 2.5

µm, which cuts parts of the band at longer wavelengths and ends up affecting the area and shape of the band, and thus also the asymmetry.

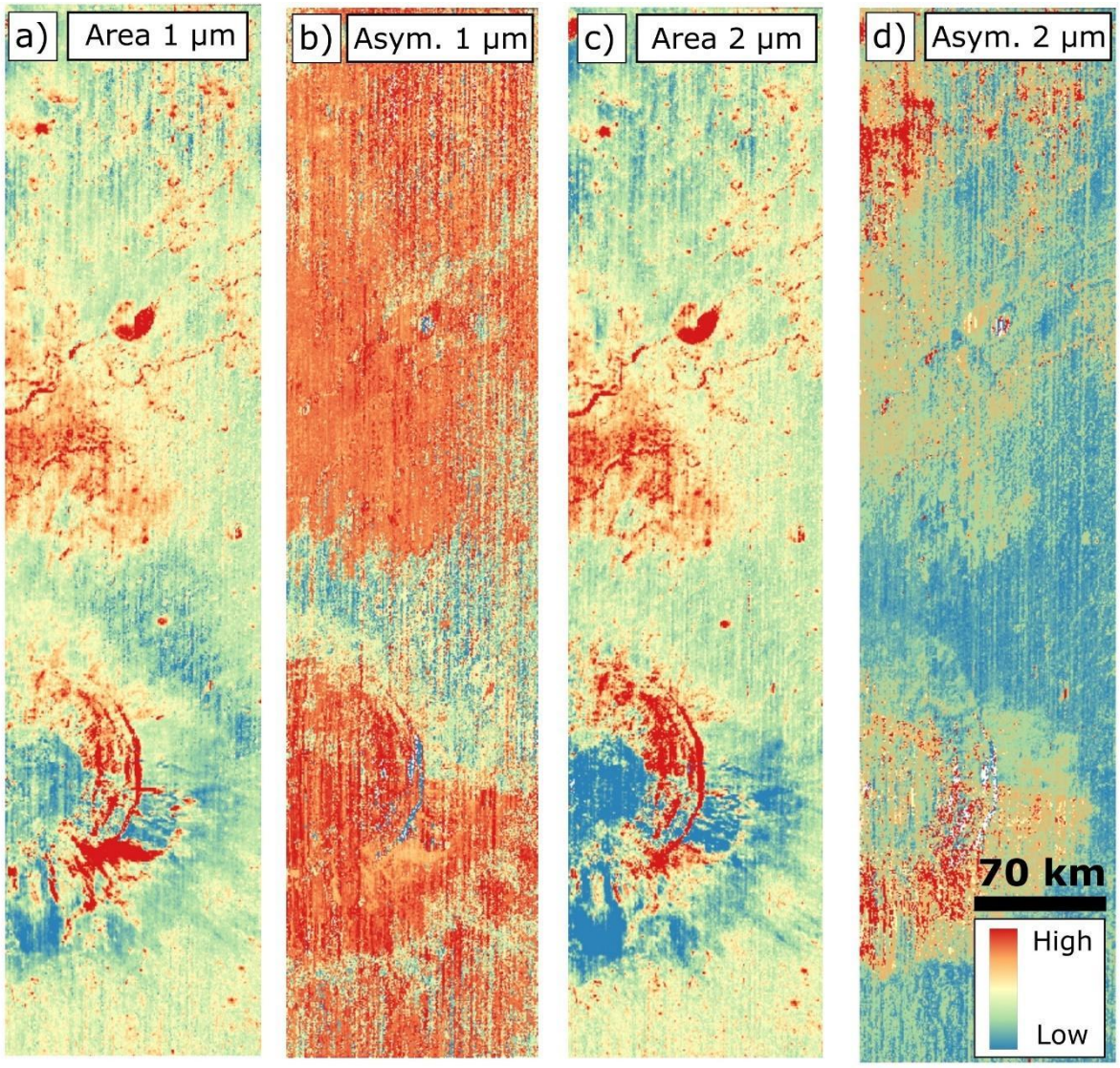

Figure 10: Band areas and asymmetries calculated by *MoonIndex* for the Aristarchus crater. a) Band area at 1 µm, the ejecta of the crater is clearly visible, the higher values, in red, indicate enrichment in OPX. b) Band asymmetry at 1 µm, higher values indicate the existence of glass-bearing ejecta. c) Band area at 2 µm, the low values at the southern part of the ejecta indicates low abundance of pyroxene. d) Band asymmetry at 2 µm, higher values also point to glass-bearing ejecta, but the widespread lower values are due to the band closing at 2.5 µm.

4.3 RGB composites

The Clementine-like color composite (Red: 750 nm/540 nm, Green: 750 nm/1000 nm, Blue:540 nm/750 nm) produced by ***MoonIndex*** for the Vallis Alpes region is showcased in

Figures 11. This composition, originally formulated by Lucey et al. (2000), displays highlands material in red, due to glass agglutinates, and maria in yellow-green due to the combination of mafic minerals signals. Our result is concordant with this distribution, since the yellow location to the south of the image corresponds to the Imbrium mare, and the red zone that covers the majority of the image is the rim of the Imbrium basin, a highlands-like terrain. A smaller linear-shaped concertation of mafic minerals is also identifiable to the north, which is related to the basaltic flood inside the Vallis Alpes.

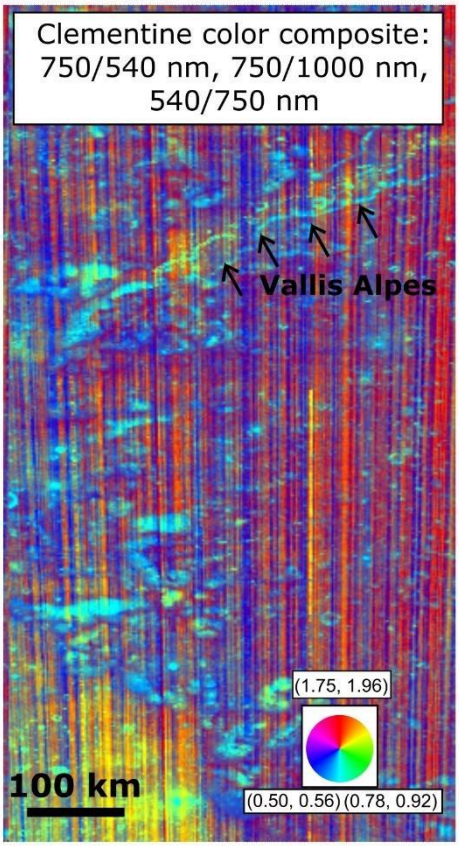

Figure 11: Clementine-like color composite created with *MoonIndex*. The red channel is 750 nm/540 nm, the green channel is 750 nm/1000 nm, and the blue channel is 540 nm/750 nm. The highlands appear in red due to the concentration of glassy agglutinates, and the maria and basaltic floods appear in yellow-green due to the combination of mafic minerals. Vallis Alpes shows a signal pointing to mafic minerals.

5 Discussion

5.1 Filtration

To evaluate the effect of the filters, we compared our results with the ones of Zambon et al. (2020) on the Apollo basin. **Figure 12** shows the band centers at 1 μm. A reduction in the number of vertical stripes is achieved with the combined filtration in MoonIndex **(Figure 12a),** this is more noticeable in the highlands around the Apollo basin, where the information of the

surface is not so distorted by vertical lines with anomalous values, as is the case for the band center of Zambon et al. (2020) **(Figure 12b)**. Furthermore, the spectral patterns of the surface are maintained after the filtering, the higher values at the center of the basin and their progressive reduction to its edges is equally recorded in both images, meaning that details were not lost. This is also true for small surface features, like the several craters in the southern highlands (black circles in **Figure 12**), which can be recognized in both versions of the index by their centering at longer wavelengths compared to their surroundings.

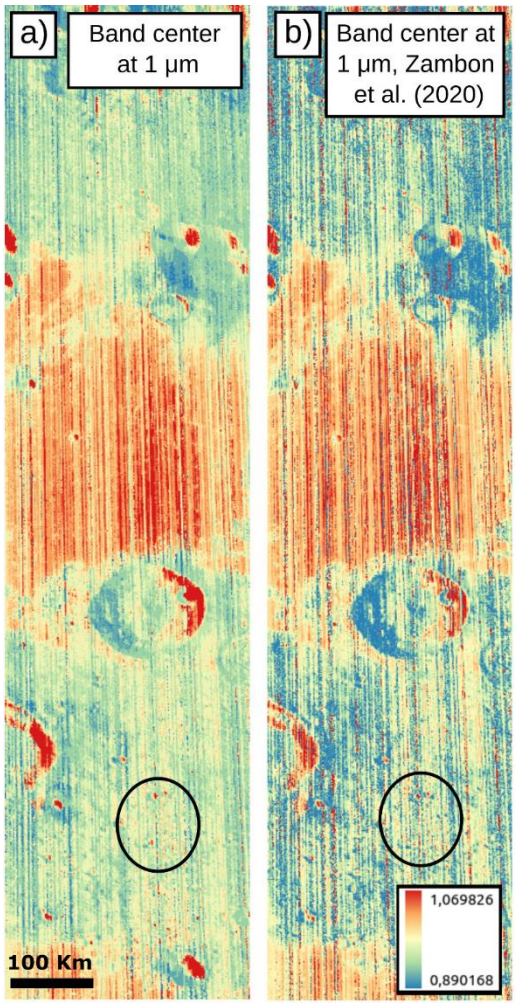

Figure 12: Band centers at 1 µm for the Apollo basin. a) Band center calculated in this work, after the Fourier and Gaussian filtrations, the number of vertical stripes is less than in a non-filtered cube, especially on the highlands. b) Band center calculated by Zambon et al. (2020). The black circles contain small craters, the signal of these geological features is maintained after the filtration, as well as the major spectral features.

5.2 Parameters

The resemblance of our parameters with the ones in the literature varies. For the indexes that are formulated before the continuum removal, such as the Clementine-like index, the results are consistent with the original data, with changes only in the spatial resolution and the noise patterns, both particular to each instrument. Nevertheless, for the indexes obtained after the

589 continuum removal, we identified variations with respect to the original formulations, which are
590 related to the methodologies used by every author. In **Figure 13** we compare our results for the
591 band center and depth at 1 μm with the ones of Zambon et al. (2020). **Figure 13a** shows the ratio
592 between the band centers, the major differences can be seen in red vertical lines and in the rims
593 of big craters. The first ones are related to the removal of vertical stripes during the filtration, and
594 the second ones to high incidence angles at the slopes of the craters. This indicates that there are
595 no major variations in the surface data, expect at particular locations inside big craters. The
596 distribution of both histograms (this work in blue, Zambon et al. (2020) in red), also reflects a
597 similar trend in both indexes (**Figure 13c**), most of the pixels in both cases are centered between
598 0.9 and 1.1 μm. Still, the band centers of Zambon et al. (2020) have a slight shift to shorter
599 wavelengths, especially in high-slope crater rims (**Figure 12b**). Major differences can be seen in
600 the ratio of the band depth at 1 μm. The red areas are widespread, and although most of them are
601 due to the destriping of our data, changes are considerable in locations with clear signals of the
602 surface (**Figure 13b**). This is further noticeable in the histograms of the band depths (**Figure**
603 **13d),** where the values of Zambon et al. (2020) accumulate more at higher values. As the band
604 area and asymmetry are both derived and linked to the band depth, our results also diverge in a
605 similar way from the ones of other authors. This major discrepancy in the band depth compared
606 to the band center is the result of using different continuum-removal methods, as we will discuss
607 later.
608

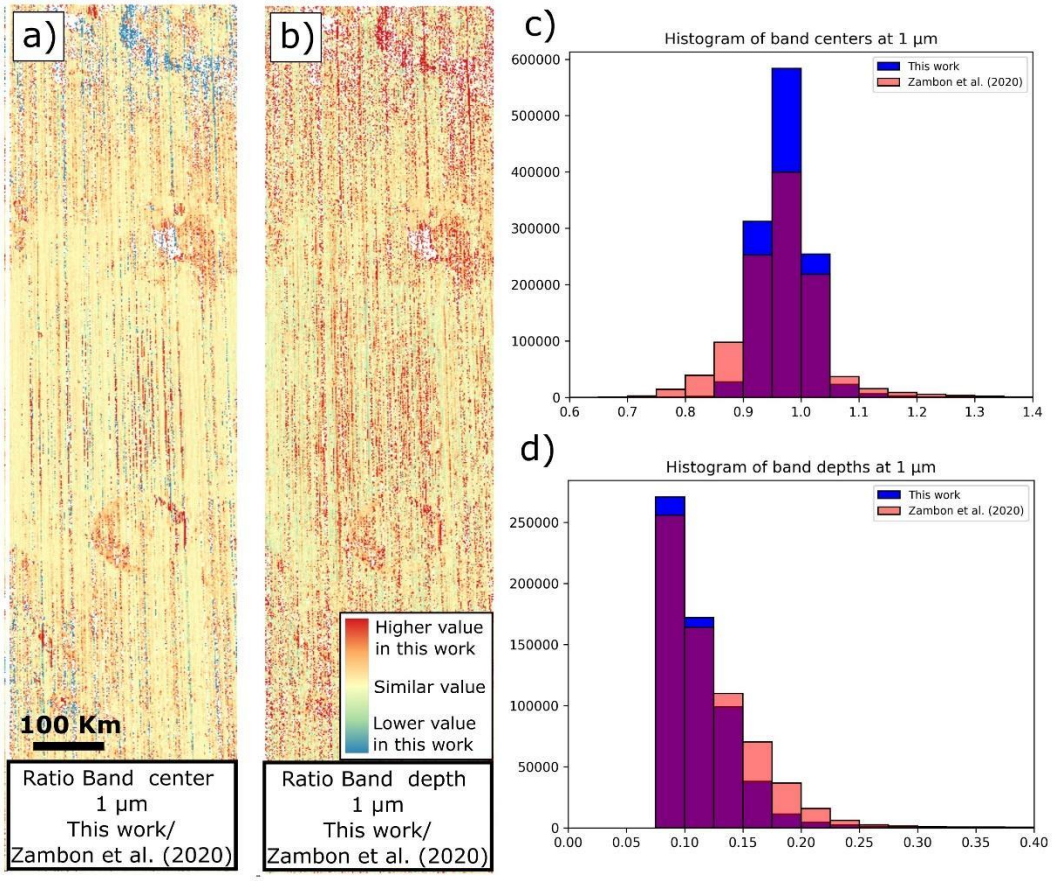

Figure 13: Comparison of our results and the ones of Zambon et al. (2020), for the band center and depth at 1 µm in the Apollo Basin. a) Ratio of the band centers, the major differences correspond to removed noise or crater rims, b) Ratio of the band depths, more discrepancies can be seen apart of the stripes and crater rims, c) Histogram of values for the band centers, trends are similar, with a small shift to smaller wavelengths in Zambon et al. (2020), d) Histogram of values for the band depths, a bigger shift is seen in this case, as the results of Zambon et al. (2020) accumulates at higher values. The difference in the counts in the histogram is due to a major amount of no data pixels in the results of Zambon et al. (2020).

5.4 Color composite maps

The comparison of our RGB color composite maps with the ones in literature presents certain difficulties. The source material from previous authors is not always available, therefore we cannot properly configure parameters like the band stretch or rendering method. Nevertheless, even when the specific colors and tonalities of the indexes may vary between works, the patterns of the geological features on the image and their differences should remain identifiable. This should allow for robust enough cartographic use of derived data.

The RGB 4 index (Red: Band center at 1 µm, Green: Band center at 2 µm, Blue: Band area at 1 µm) recreated in this work is close to the original one produced by Horgan et al. (2014) (**Figure 14a and 14b**) for the Aristarchus crater. The main colors are maintained, and the

geological features are easily recognizable. This index is particularly useful to differentiate between pyroxenes, OPX is seen in blue, CPX in yellow, and a mix between them is green. Ejecta glass is also visible in magenta and orange. Although both indexes are generally compatible, there are some differences in the distribution. In our results the blue areas are smaller, indicating a lesser amount of OPX in the ejecta blanket. The black regions on the original index are pink in our work, which correspond to shadows or melt with no major signal around the 1 μm band. On the other hand, the differences are bigger for the RGB 5 (Red: Band asymmetry at 1 μm, Green: Band center at 1 μm, blue: Band center at 2 μm), also originally formulated by Horgan et al. (2014) (**Figure 14c and 14d**). This index is intended to highlight glass-bearing lithologies due to their high asymmetries, which will appear in pink and yellow. Both indexes are consistent north of the Aristarchus crater; the large pink area north of the crater is followed by the yellow-dominated locations. To the south, the results of Horgan et al. (2014) show lesser amounts of glass, while ours have a pink area that fits well with the ejecta blanket of the crater.

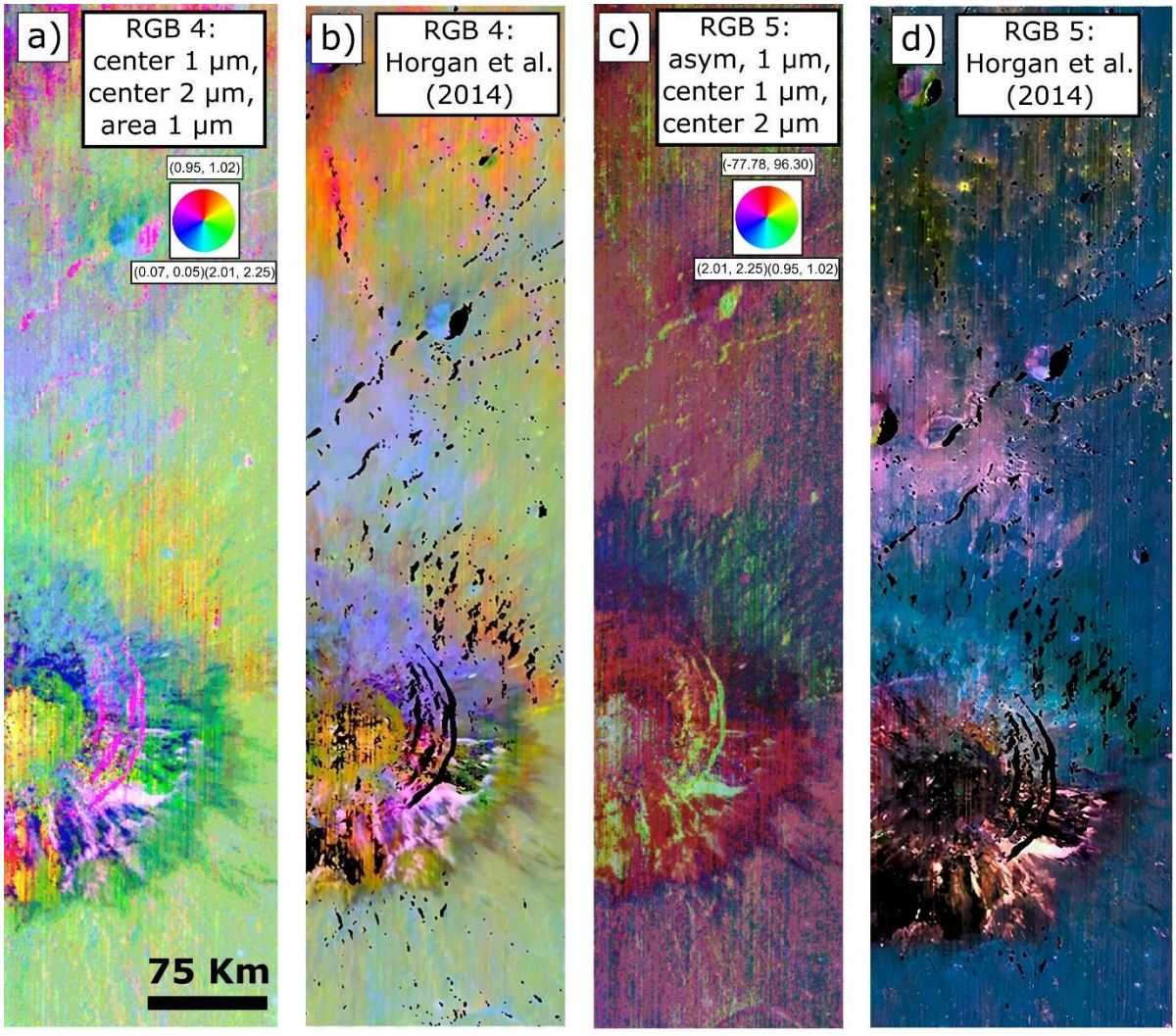

Figure 14: Comparison between our results and the ones of Horgan et al. (2014) for the Aristarchus crater. a) RGB 4 recreated in this work, the red channel is the band center at 1

µm, green is the band center 2 µm, and blue is the band area at 1 µm. b) original RGB 4 by Horgan et al. (2014), both color ramps are consistent, and the ejecta blanket and its compositional variation are seen in both cases, blue implies OPX, yellow CPX and green a mix of both. c) RGB 5 recreated in this work, the red channels are the band asymmetry at 1 µm, green is the band center at 1 µm, and blue is the band center at 2 µm; overlaid by the band area at 1 µm in grayscale. d) original formulation of the RGB 5 by Horgan et al. (2014), the color ramp is less consistent, especially at the ejecta south of the crater, nevertheless the distribution of glass-bearing rocks (yellow and pink) is consistent north of the crater. The stretch values of Horgan et al. (2014) are unknown.

Another index worth comparing is RGB 8 (Red: Band depth at 1.9 µm, Green: IBD at 2 µm, Blue: IBD at 1 µm), originally formulated by Bretzfelder et al. (2020) for the Vallis Alpes region. On the original index, yellow corresponds to OPX, cyan to CPX, and most important, dark blue shows olivine-bearing massifs. Our results show a different color ramp (**Figure 15**). This occurs because we used a modified method to calculate the band depth at 1.9 µm; instead of creating a specific continuum for the band, we measure the depth directly on the convex-hull removed spectra. But even if the calculation and the resulting color ramp are different, the same geological patterns are still identifiable in both composites. In our results, CPX is still yellow, OPX is light blue, and olivine-bearing rocks appear purple. An example of the last is the isolated mountain next to the southern edge of Vallis Alpes, which shows a strong olivine signal in both indexes (**Figure 15**). Since this index was thought specially to identify olivine, our result is still relevant and applicable for that purpose.

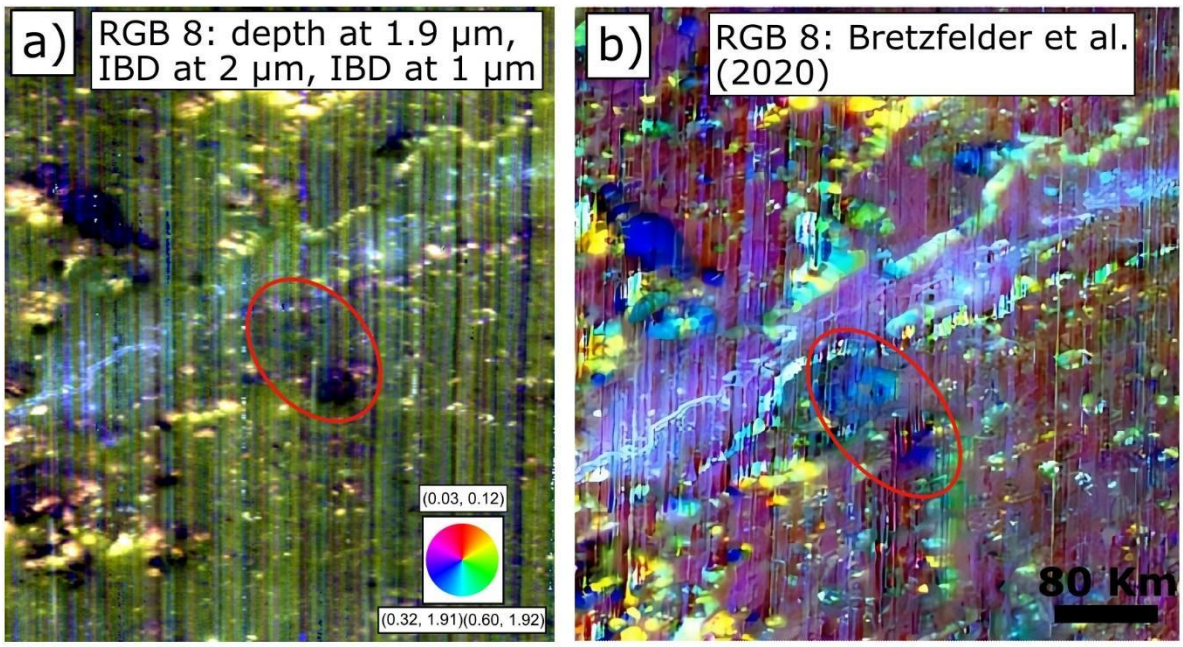

Figure 15: Comparison between our results and the ones of Horgan et al. (2020) for the Vallis Alpes. a) RGB 8 recreated in this work, red is the band depth at 1.9 µm, green is IBD at 2 µm, and blue is IBD at 1 µm. b) original formulation of the RGB 8 by Bretzfelder et al. (2020). Stretch values are unknown. The ramp color is different in both cases, due to a change in the calculation of the band depth at 1.9 µm. Nevertheless, the pattern of

geological features is maintained, for example the dark blue spots on the original index correspond to olivine (red circle), and in our recreation those same areas appear purple.

5.5 Effect of the continuum-removal method

The differences between our results and the ones of the previous authors are produced by several factors. The method used to remove the continuum is the main variable affecting the indexes. Since most of the previous authors used a combination of linear fits and second-order fits within defined intervals (Horgan et al., 2014, Zambon et al., 2020), a comparison between the results of our convex hull and linear-fit methods is helpful to explain the changes.

The general shape of the resulting continuum-removed spectrum is similar in both methods (**Figure 16a**), and all the parameters of the absorption bands are well represented and easily measurable. The band center is not greatly affected by the removal method; the average difference between both procedures is 5 nm at the 1 μm absorption band, and 25 nm at the 2 μm band, which is in both cases smaller than the spectral sampling of M^3 for those regions. On the other hand, the band depth is especially sensitive to the selected method, which can be appreciated by subtracting the images (**Figure 16b**). At 1 μm the band depth varies considerably, higher values are obtained with the linear-fit method in the highlands (**Figure 16a**), while in the mare the result is the opposite (**Figure 16c**). This inconsistency is the result of the way in which both methods define the continuum line. The linear fit interpolates a second order polynomial function between two arbitrarily defined shoulders, while the convex hull draws a straight line connecting the local maximums it automatically computes (**Figure 8**). Hence, when the absorption band is weak, like on the highlands, the concave shape of the linear fit method creates a slightly higher distance to the spectrum, resulting in bigger band depth values (**Figure 16d**). As for the maria regions, it looks like the convex hull method is identifying the right shoulder at longer wavelengths, which produces a deeper band depth. The band depth at 2 μm is less affected by the method, the variation is lower than in the 1 μm band, and most of the values are inside one standard deviation (**Figure 16e**). The linear-fit method uses a straight line for the 2 μm absorption band, thus the result is closer to the also linear interpolation done by the convex hull. Subsequent indexes like the band area and asymmetry are also affected in similar ways, especially at the 1 μm absorption bands, as larger band depths will result in larger band areas.

Several other factors are surely responsible for changes on the resulting indexes, but the lack of source materials for some of the indexes makes them difficult to evaluate. During the preprocessing of the data many factors could change, if the authors applied custom filtrations or workflows before calculating the indexes, that would affect the end-result. Another difficulty is added to the RGB composites, even if the formulations are similar, we cannot be sure of the color stretch or the display settings of the original indexes. Small changes in the intervals of the values displayed by each channel can greatly modify the color ramp of a composite. In any case, the geological and spectral features on our composites are consistent with the original ones regardless of their tonality, so the products of ***MoonIndex*** appear to be reliable for geological analysis.

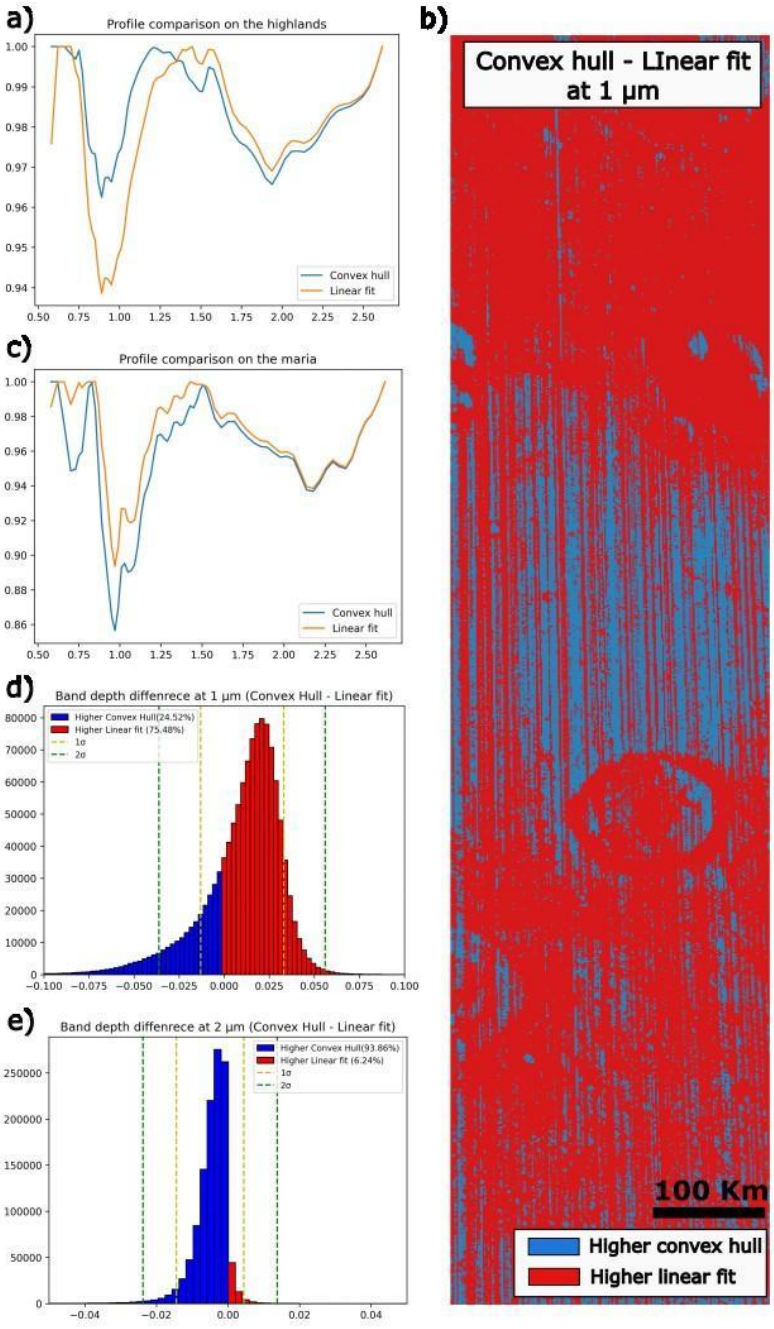

713

714 **Figure 16: Comparison between the band depth results of the convex hull and the**
715 **linear-fit methods for the Apollo basin. a) Spectral profiles of the same pixel on the**
716 **highlands using the two methods, the bandh depth is greater with the linear-fit method. b)**
717 **Image showing the difference between the results of the linear fit and the convex hull**
718 **methods, in red regions where the linear-fit returned higher values, in blue the opposite. c)**
719 **Spectral profiles on the mare, this time the convex hull has a higher band depth. d)**
720 **Histogram of the values at 1 µm, the values are scattered more than two standard**
721 **deviations. e) Histogram of the values at 2 µm, the difference between both methods is close**
722 **to zero, and the values are not so scattered.**

The reconstruction of spectral indexes from such varied sources makes it difficult to accomplish a high fidelity in all of them. This is especially true when some of those indexes were formulated several years ago, with different missions, methodologies, and technologies. Nevertheless, our methodologies and results are consistent with each other, so the analyses derived from them are complementary and comparable. Given this context, consistency between the data is important when applied to the geological analysis of a region on the Moon, so we recommend the users of ***MoonIndex*** to use only one of the continuum removal methods for each project they might work on.

6 Conclusions

Spectral indexes are an easy way to approach the compositional analysis of the Moon. Even if there is no unified list of them for M^3, the highly homogeneous composition of the Moon and the broad spectral coverage of M^3 allow the reusability of indexes defined for previous instruments, and the creation of new ones taking advantage of the better spectral resolution. During our recreation of the spectral indexes in python we added certain improvements to the workflow. The gaussian and Fourier filtrations proved useful to reduce the vertical striping typical of M^3 data, allowing the extraction of more geological information, especially from cubes that otherwise would be almost useless for scientific purposes. The implementation of the convex hull method to remove the spectral continuum has certain advantages over the linear-fit method; as the method creates an envelope over all the local maximums, all the absorption bands present on the spectrum should be identified. Furthermore, the convex hull works automatically over the data, removing the necessity of establishing arbitrary limits for the interpolations, and thus reducing the human error in the process. We recommend the use of the convex hull method over the linear-fit method, but both are still implemented in ***MoonIndex***.

The fidelity of the reconstructed indexes varies for several reasons. The most important one is related to the continuum removal method used in this work, but other unknown factors like the preprocessing, filtration, or the visualization parameters of the composites, are likely altering the results. Nevertheless, in all cases the reproduced indexes have a similar scientific meaning, and they highlight the same compositional properties as the original formulation, even if the tonality or values change. The products of ***MoonIndex*** are consistent with each other, but the processing particularities described in this work should be considered when comparing them with indexes from other works.

The versatility of spectral indexes allows certain freedom when interpreting them. **Table 1** highlights the indexes found in literature, but further combinations or operations can be made with the products of ***MoonIndex***, we recommend the user to generate custom composites according to their needs.

Finally, ***MoonIndex*** was created to give a better accessibility to this kind of product to the scientific community. The package is Open-Source and freely available, so that users can modify it for their own purposes. The necessity to preprocess the data in other not-so-intuitive software like ISIS and GDAL may make the task difficult, but other tools like the EXPLORE platform or the GMAP Jupyter Hub (Nodjoumi et al., 2022), could contribute to ease the process.

Acknowledgments

This research was done on the framework of the EXPLORE project, that has received funding from the European Union's 2020 research and innovation program under grant agreement No 101004214. Additionally, we had support from the GMAP project, part of the Europlanet 2024 RI has received funding from the European Union's Horizon 2020 research and innovation programme under grant agreement No 871149.

Open Research

MoonIndex is available for Python 3.12 in the PyPI repository. The tool is released under the GNU general public license. The source code, exemplary Jupyter notebooks, definition of functions, and workflows can be accessed via GitHub and Zenodo (https://zenodo.org/records/10036999). The raw datasets used in this work can be accessed through the PDS, and versions ready to use on ***MoonIndex*** are reachable at https://zenodo.org/records/10014564.

References

Acton, C., Bachman, N., Semenov, B., & Wright, E. (2016). SPICE TOOLS SUPPORTING PLANETARY REMOTE SENSING. *The International Archives of the Photogrammetry, Remote Sensing and Spatial Information Sciences*, *XLI-B4*, 357-359. https://doi.org/10.5194/isprs-archives-XLI-B4-357-2016

Adams, J. B. (1974). Visible and near-infrared diffuse reflectance spectra of pyroxenes as applied to remote sensing of solid objects in the solar system. Journal of Geophysical Research, 79(32), 4829–4836. https://doi.org/10.1029/jb079i032p04829

Adams, J. B. & Filice, A. L. (1967). Spectral reflectance 0.4 to 2.0 microns of silicate rock powders. Journal of Geophysical Research, 72(22), 5705–5715. https://doi.org/10.1029/jz072i022p05705

Adams, J. B. & McCord, T. B. (1971). Alteration of Lunar Optical Properties: Age and composition effects. Science , 171 (3971), 567–571. https://doi.org/10.1126/science.171.3971.567

Agrell, S. O., Scoon, J. H., Muir, I. D., Long, J. V. P., McConnell, J. D., & Peckett, A. (1970). Observations on the chemistry, mineralogy and petrology of some Apollo 11 lunar samples. *Geochimica et Cosmochimica Acta Supplement*, *1*, 93.

Albee, A. L. (2003). Lunar Rocks. In Elsevier eBooks (S. 825–837). https://doi.org/10.1016/b0-12-227410-5/00390-2

Arnold, J. A., Glotch, T. D., Lucey, P. G., Song, E., Thomas, I. R., Bowles, N. E., & Greenhagen, B. T. (2016). Constraints on olivine-rich rock types on the Moon as observed by Diviner and M ^{3}: Implications for the

formation of the lunar crust: CONSTRAINTS ON OLIVINE-RICH ROCK TYPES ON THE MOON. *Journal of Geophysical Research: Planets*, *121*(7), 1342-1361. https://doi.org/10.1002/2015JE004874

Besse, S., Sunshine, J. M., Staid, M. I., Petro, N. E., Boardman, J. W., Green, R. O., Head, J. W., Isaacson, P. J., Mustard, J. F., & Pieters, C. M. (2011). Compositional variability of the Marius Hills volcanic complex from the Moon Mineralogy Mapper (M^3). *Journal of Geophysical Research*, *116*, E00G13. https://doi.org/10.1029/2010JE003725

Bradski, G. (2000). The OpenCV Library. *Dr. Dobb's Journal of Software Tools*.

Bretzfelder, J. M., Klima, R. L., Greenhagen, B. T., Buczkowski, D. L., Petro, N. E., & Day, M. (2020). Identification of Potential Mantle Rocks Around the Lunar Imbrium Basin. *Geophysical Research Letters*, *47*(22). https://doi.org/10.1029/2020GL090334

Burns, R. G. (1993). Mineralogical applications of Crystal field Theory. https://doi.org/10.1017/cbo9780511524899

Cheek, L. C., Hanna, K. L. D., Pieters, C. M., Head, J. W. & Whitten, J. L. (2013). The distribution and purity of anorthosite across the Orientale Basin: New perspectives from Moon Mineralogy Mapper Data. *Journal of Geophysical Research: Planets*, *118*(9), 1805–1820. https://doi.org/10.1002/jgre.20126

Chevrel, S., Pinet, P., Daydou, Y., Mouëlic, SL, Langevin, Y., Costard, F. & Erard, S. (2009). The Aristarchus plateau on the Moon: Mineralogical and structural study from Integrated Clementine UV–VIS–NIR Spectral data. Icarus , 199 (1), 9–24. https://doi.org/10.1016/j.icarus.2008.08.005

Clark, R. N. & Roush, T. L. (1984c). Reflectance Spectroscopy: quantitative analysis techniques for remote sensing applications. Journal of Geophysical Research, 89(B7), 6329–6340. https://doi.org/10.1029/jb089ib07p06329

Clenet, H. (2009). *Télédétection hyperspectrale: Minéralogie et pétrologie, Application au volcan Syrtis Major (Mars) et à l'ophiolite d'Oman*. Université de Toulouse.

Cloutis, E. A., Gaffey, M. J., Jackowski, T. L. & Reed, K. L. (1986). Calibrations of phase abundance, composition, and particle size distribution for olivine-orthopyroxene mixtures from reflectance spectra. Journal of Geophysical Research, 91(B11), 11641. https://doi.org/10.1029/jb091ib11p11641

Cloutis, E. A., Gaffey, M. J., Smith, D. G. & St J Lambert, R. (1990). Reflectance spectra of glass-bearing mafic silicate mixtures and spectral deconvolution procedures. Icarus, 86(2), 383–401. https://doi.org/10.1016/0019-1035(90)90226-y

Cloutis, E. A., Sunshine, J. M., & Morris, R. V. (2004). Spectral reflectance-compositional properties of spinels and chromites: Implications for planetary remote sensing and geothermometry. *Meteoritics & Planetary Science*, *39*(4), 545-565. https://doi.org/10.1111/j.1945-5100.2004.tb00918.x

Corley, L. M., McGovern, P. J., Kramer, G. Y., Lemelin, M., Trang, D., Gillis-Davis, J. J., Taylor, G. J., Powell, K. E., Kiefer, W. S., Wieczorek, M., & Zuber, M. T. (2018). Olivine-bearing lithologies on the Moon: Constraints on origins and transport mechanisms from M3 spectroscopy, radiative transfer modeling, and GRAIL crustal thickness. *Icarus*, *300*, 287-304. https://doi.org/10.1016/j.icarus.2017.09.012

Figuera, R. M., Huu, B. P., Rossi, A. P., Minin, M., Flahaut, J. & Halder, A. (2018). Online characterization of planetary surfaces: PlanetServer, an open-source analysis and visualization tool. Planetary and Space Science, 150, 141–156. https://doi.org/10.1016/j.pss.2017.09.007

Gillies, S. & others. (2013). *Rasterio: Geospatial raster I/O for Python programmers*. Mapbox. https://github.com/mapbox/rasterio

Graham, R. L. (1972). An efficient algorith for determining the convex hull of a finite planar set. *Information Processing Letters*, *1*(4), 132-133. https://doi.org/10.1016/0020-0190(72)90045-2

Green, R. O., Pieters, C., Mouroulis, P., Eastwood, M., Boardman, J., Glavich, T., Isaacson, P., Annadurai, M., Besse, S., Barr, D., Buratti, B., Cate, D., Chatterjee, A., Clark, R., Cheek, L., Combe, J., Dhingra, D., Essandoh, V., Geier, S., … Wilson, D. (2011). The Moon Mineralogy Mapper (M^3) imaging spectrometer for lunar science: Instrument description, calibration, on-orbit measurements, science data calibration and on-orbit validation. *Journal of Geophysical Research*, *116*, E00G19. https://doi.org/10.1029/2011JE003797

Hapke, B. (1993). *Theory of Reflectance and Emittance Spectroscopy* (1.ª ed.). Cambridge University Press. https://doi.org/10.1017/CBO9780511524998

Hapke, B. (2001). Space weathering from Mercury to the asteroid Belt. *Journal of Geophysical Research*, *106*(E5), 10039–10073. https://doi.org/10.1029/2000je001338

Harris, C. R., Millman, K. J., Van Der Walt, S. J., Gommers, R., Virtanen, P., Cournapeau, D., Wieser, E., Taylor, J., Berg, S., Smith, N. J., Kern, R., Picus, M., Hoyer, S., Van Kerkwijk, M. H., Brett, M., Haldane, A., Del Río, J. F., Wiebe, M., Peterson, P., … Oliphant, T. E. (2020). Array programming with NumPy. *Nature*, *585*(7825), 357-362. https://doi.org/10.1038/s41586-020-2649-2

Hazen, R. M., Mao, H. K. & Bell, P. M. (1978). Effects of compositional variation on absorption spectra of lunar pyroxenes. Lunar and Planetary Science Conference Proceedings, 1, 1081–1090. https://ntrs.nasa.gov/search.jsp?R=19780057713

Hiesinger, H. & Head, J. W. (2006). New Views of Lunar Geoscience: An Introduction and Overview. Reviews in mineralogy and geochemistry, 60(1), 1–81. https://doi.org/10.2138/rmg.2006.60.1

Horgan, B. H. N., Cloutis, E. A., Mann, P., & Bell, J. F. (2014). Near-infrared spectra of ferrous mineral mixtures and methods for their identification in planetary surface spectra. *Icarus*, *234*, 132-154. https://doi.org/10.1016/j.icarus.2014.02.031

Hoyer, S., & Joseph, H. (2017). xarray: N-D labeled Arrays and Datasets in Python. *Journal of Open Research Software*, *5*(1). https://doi.org/10.5334/jors.148

Hunter, J. D. (2007). Matplotlib: A 2D Graphics Environment. *Computing in Science & Engineering*, *9*(3), 90-95. https://doi.org/10.1109/MCSE.2007.55

Ivanov, M. A., Hiesinger, H., Van Der Bogert, C. H., Orgel, C., Pasckert, J. H., & Head, J. W. (2018). Geologic History of the Northern Portion of the South Pole-Aitken Basin on the Moon. *Journal of Geophysical Research: Planets*, *123*(10), 2585-2612. https://doi.org/10.1029/2018JE005590

Isaacson, P., Pieters, C. M., Besse, S., Clark, R. N., Head, J. W., Klima, R. L., Mustard, J. F., Petro, N. E., Staid, M., Sunshine, J. M., Taylor, L. A., Thaisen, K. G. & Tompkins, S. (2011). Remote Compositional Analysis of Lunar Olivine-rich Lithologies with Moon Mineralogy Mapper (M3) Spectra. Journal of Geophysical Research, 116. https://doi.org/10.1029/2010je003731

Karr, C. (1975). Infrared and Raman spectroscopy of lunar and terrestrial minerals. In *Elsevier eBooks*. https://doi.org/10.1016/c2013-0-10938-5

Klima, R. L., Pieters, C. M., Boardman, J. W., Green, R. O., Head, J. W., Isaacson, P. J., Mustard, J. F., Nettles, J. W., Petro, N. E., Staid, M. I., Sunshine, J. M., Taylor, L. A., & Tompkins, S. (2011). New insights into lunar petrology: Distribution and composition of prominent low-Ca pyroxene exposures as observed by the Moon Mineralogy Mapper (M^3). *Journal of Geophysical Research*, *116*, E00G06. https://doi.org/10.1029/2010JE003719

Klima, R. L., Pieters, C. M., & Dyar, M. D. (2007). Spectroscopy of synthetic Mg-Fe pyroxenes I: Spin-allowed and spin-forbidden crystal field bands in the visible and near-infrared. *Meteoritics & Planetary Science*, *42*(2), 235-253. https://doi.org/10.1111/j.1945-5100.2007.tb00230.x

Klima, R. L., Dyar, M. D. & Pieters, C. M. (2011). Near-infrared spectra of clinopyroxenes: effects of calcium content and crystal structure. *Meteoritics & Planetary Science*, *46*(3), 379–395. https://doi.org/10.1111/j.1945-5100.2010.01158.x

Laura, J., Acosta, A., Addair, T., Adoram-Kershner, L., Alexander, J., Alexandrov, O., Alley, S., Anderson, D., Anderson, J., Anderson, J., Annex, A., Archinal, B., Austin, C., Backer, J., Barrett, J., Bauck, K., Bauers, J., Becker, K., Becker, T., … Young, A. (2023). *Integrated Software for Imagers and Spectrometers* (7.2.0_RC1) [Software]. Zenodo. https://doi.org/10.5281/ZENODO.2563341

Lawrence, D. J., Feldman, W. C., Barraclough, B. L., Binder, A. B., Elphic, R. C., Maurice, S., & Thomsen, D. R. (1998). Global Elemental Maps of the Moon: The Lunar Prospector Gamma-Ray Spectrometer. *Science*, *281*(5382), 1484-1489. https://doi.org/10.1126/science.281.5382.1484

Lemelin, M., Lucey, P. G. & Camon, A. (2022). Compositional maps of the lunar polar regions derived from the Kaguya Spectral Profiler and the Lunar Orbiter Laser Altimeter data. *The planetary science journal*, *3*(3), 63. https://doi.org/10.3847/psj/ac532c

Liu, J. G., & Mason, P. J. (2009). *Essential Image Processing and GIS for Remote Sensing* (1.ª ed.). Wiley. https://doi.org/10.1002/9781118687963

Lucey, P. G., Blewett, D. T., & Jolliff, B. L. (2000). Lunar iron and titanium abundance algorithms based on final processing of Clementine ultraviolet-visible images. *Journal of Geophysical Research: Planets*, *105*(E8), 20297-20305. https://doi.org/10.1029/1999JE001117

Lucey, P. G., Blewett, D. T., Taylor, G. J., & Hawke, B. R. (2000). Imaging of lunar surface maturity. *Journal of Geophysical Research: Planets*, *105*(E8), 20377-20386. https://doi.org/10.1029/1999JE001110

Lucey, P. G., Greenhagen, B., Donaldson Hanna, K., Bowles, N., Flom, A., & Paige, D. A. (2021). Christiansen Feature Map From the Lunar Reconnaissance Orbiter Diviner Lunar Radiometer Experiment: Improved Corrections and Derived Mineralogy. *Journal of Geophysical Research: Planets*, *126*(6). https://doi.org/10.1029/2020JE006777

Lundeen, S., McLaughlin, S., & Alanis, R. (2011). *Moon MIneralogy Mapper Data Product Doftware Interface Specification* (39032; p. 111). JPL.

Malaret, E., P. Guasqui, S. McLaughlin, J. Sunshine, S. Besse, R. Clark, and P. Isaacson, CH1-ORB MOON M3 4 L2 REFLECTANCE NEAR-IR SPECTRAL IMAGES V1.0, CH1-ORB-L-M3-4-L2-REFLECTANCE-V1.0, NASA Planetary Data System, 2011. https://doi.org/10.17189/1520414

McCord, T. B., Charette, M. P., Johnson, T. V., Lebofsky, L. A., Pieters, C., & Adams, J. B. (1972). Lunar spectral types. *Journal of Geophysical Research*, *77*(8), 1349-1359. https://doi.org/10.1029/JB077i008p01349

Montero, D., Aybar, C., Mahecha, M. D., Martinuzzi, F., Söchting, M., & Wieneke, S. (2023). A standardized catalogue of spectral indices to advance the use of remote sensing in Earth system research. *Scientific Data*, *10*(1), 197. https://doi.org/10.1038/s41597-023-02096-0

Moriarty, D. P., Simon, S. B., Shearer, C. K., Haggerty, S. E., Petro, N., & Li, S. (2023). Orbital Characterization of the Composition and Distribution of Spinels Across the Crisium Region: Insight From Luna 20 Samples. *Journal of Geophysical Research: Planets*, *128*(5), e2022JE007482. https://doi.org/10.1029/2022JE007482

Mustard, J. F., Pieters, C. M., Isaacson, P. J., Head, J. W., Besse, S., Clark, R. N., Klima, R. L., Petro, N. E., Staid, M. I., Sunshine, J. M., Runyon, C. J., & Tompkins, S. (2011). Compositional diversity and geologic insights of the Aristarchus crater from Moon Mineralogy Mapper data. *Journal of Geophysical Research*, *116*, E00G12. https://doi.org/10.1029/2010JE003726

Nodjoumi, G., Brandt, C., & Rossi, A. P. (2022, junio). *OPEN-SOURCE PLANETARY DATA PROCESSING ENVIRONMENTS BASED ON JUPYTERHUB AND DOCKER CONTAINERS*.

Nozette, S. (1995). The Clementine mission: Past, present, and future. *Acta Astronautica*, *35*, 161-169. https://doi.org/10.1016/0094-5765(94)00181-K

Moriarty, D. P., & Pieters, C. M. (2018). The character of South Pole-Aitken Basin: Patterns of surface and subsurface composition. Journal of Geophysical Research: Planets, 123(3), 729-747. https://doi.org/10.1002/2017je005364

Ohtake, M., Matsunaga, T., Haruyama, J., Yokota, Y., Morota, T., Honda, C., Ogawa, Y., Torii, M., Miyamoto, H., Arai, T., Hirata, N., Iwasaki, A., Nakamura, R., Hiroi, T., Sugihara, T., Takeda, H., Otake, H., Pieters, C. M., Saiki, K., . . . Josset, J. (2009). The global distribution of pure anorthosite on the moon. Nature, 461(7261), 236–240. https://doi.org/10.1038/nature08317

Pieters, C. M., Boardman, J., Buratti, B., Chatterj, A., Clark, R., Glavich, T., Green, R., Malaret, E., McCord, T., Mustard, J., Petro, N., Runyon, C., Staid, M., Sunshine, J., Tay, L., Tompkins, S., Varanasi, P., & White, M. (2009). *The Moon Mineralogy Mapper (M^3) on Chandrayaan-1*.

Pieters, C. M., Goswami, J. N., Clark, R. N., Annadurai, M., Boardman, J., Buratti, B., Combe, J.-P., Dyar, M. D., Green, R., Head, J. W., Hibbitts, C., Hicks, M., Isaacson, P., Klima, R., Kramer, G., Kumar, S., Livo, E., Lundeen, S., Malaret, E., … Varanasi, P. (2009). Character and Spatial Distribution of OH/H $_2$ O on the Surface of the Moon Seen by M ^{3} on Chandrayaan-1. *Science*, *326*(5952), 568-572. https://doi.org/10.1126/science.1178658

Pieters, C. M., Hanna, K. L. D., Cheek, L. C., Dhingra, D., Prissel, T. C., Jackson, C. R., Moriarty, D. P., Parman, S. W. & Taylor, L. A. (2014). The distribution of MG-spinel across the moon and constraints on crustal origin. American Mineralogist, 99(10), 1893–1910. https://doi.org/10.2138/am-2014-4776

Prissel, T. C., & Prissel, K. B. (2021). A lunar sample renaissance. *Nature Communications*, *12*(1), 7053. https://doi.org/10.1038/s41467-021-27296-3

Potter, R. W. K., Head, J. W., Guo, D., Liu, J., & Xiao, L. (2018). The Apollo Peak-Ring Impact Basin: Insights into the structure and evolution of the South Pole–Aitken Basin. Icarus, 306, 139-149. https://doi.org/10.1016/j.icarus.2018.02.007

Rouault, E., Warmerdam, F., Schwehr, K., Kiselev, A., Butler, H., Łoskot, M., Szekeres, T., Tourigny, E., Landa, M., Miara, I., Elliston, B., Chaitanya, K., Plesea, L., Morissette, D., Jolma, A., & Dawson, N. (2023). *GDAL* (v3.7.1) [Software]. Zenodo. https://doi.org/10.5281/ZENODO.5884351

Sasaki, S., Iijima, Y., Tanaka, K., Kato, M., Hashimoto, M., Mizutani, H., & Takizawa, Y. (2003). The SELENE mission: Goals and status. *Advances in Space Research*, *31*(11), 2335-2340. https://doi.org/10.1016/S0273-1177(03)00543-X

Serventi, G., Carli, C., Sgavetti, M., Ciarniello, M., Capaccioni, F. & Pedrazzi, G. (2013). Spectral variability of plagioclase–mafic mixtures (1): effects of chemistry and modal abundance in reflectance spectra of rocks and mineral mixtures. *Icarus*, *226*(1), 282–298. https://doi.org/10.1016/j.icarus.2013.05.041

Shearer, C. K., Elardo, S. M., Petro, N. E., Borg, L. E., & McCubbin, F. M. (2015). Origin of the lunar highlands Mg-suite: An integrated petrology, geochemistry, chronology, and remote sensing perspective. *American Mineralogist*, *100*(1), 294-325. https://doi.org/10.2138/am-2015-4817

Shkuratov, Yu., Surkov, Ye., Ivanov, M., Korokhin, V., Kaydash, V., Videen, G., Pieters, C., & Stankevich, D. (2019). Improved Chandrayaan-1 M3 data: A northwest portion of the Aristarchus Plateau and contiguous maria. *Icarus*, *321*, 34-49. https://doi.org/10.1016/j.icarus.2018.11.002

Suarez-Valencia, J. (2023). Javierunal16/MoonIndex: First version of the MoonIndex package. (1.0). Zenodo. https://doi.org/10.5281/zenodo.10036999

Sunshine, J. M., & Pieters, C. M. (1998). Determining the composition of olivine from reflectance spectroscopy. *Journal of Geophysical Research: Planets*, *103*(E6), 13675-13688. https://doi.org/10.1029/98JE01217

Sunshine, J. M., Pieters, C. M., & Pratt, S. F. (1990). Deconvolution of mineral absorption bands: An improved approach. *Journal of Geophysical Research*, *95*(B5), 6955. https://doi.org/10.1029/JB095iB05p06955

Taylor, G. J. (1972). The composition of the lunar highlands: Evidence from modal and normative plagioclase contents in anorthositic lithic fragments and glasses. *Earth and Planetary Science Letters*, *16*(2), 263-268. https://doi.org/10.1016/0012-821X(72)90200-2

Taylor, S. R. (1976). *Geochemical Constraints on the Composition of the Moon*. *7*, 855.

Warren, P. H. & Korotev, R. L. (2022). Ground truth constraints and remote sensing of Lunar Highland crust composition. Meteoritics & Planetary Science, 57(2), 527–557. https://doi.org/10.1111/maps.13780

Wu, Y., Xue, B., Zhao, B., Lucey, P., Chen, J., Xu, X., Li, C., & Ouyang, Z. (2012). Global estimates of lunar iron and titanium contents from the Chang' E-1 IIM data: LUNAR Fe AND Ti FROM CHANG'E-1 IIM DATA. *Journal of Geophysical Research: Planets*, *117*(E2), n/a-n/a. https://doi.org/10.1029/2011JE003879

Zambon, F., Carli, C., Altieri, F., Luzzi, E., Combe, J.-P., Ferrari, S., Tognon, G., & Massironi, M. (2020). *Spectral Index and RGB maps—Beethoven, Rembrandt basins on Mercury, Apollo basin and Leibnitz and Von Karman craters regions on the Moon* (p. 57).

Zhang, X.-Y., Ouyang, Z.-Y., Zhang, X.-M., Chen, Y., Tang, X., Xu, A.-A., Tang, Z.-S., & Wu, Y.-Z. (2016). Study of the continuum removal method for the Moon Mineralogy Mapper (M^3) and its application to Mare Humorum and Mare Nubium. *Research in Astronomy and Astrophysics*, *16*(7), 015. https://doi.org/10.1088/1674-4527/16/7/115

Xu, J., Mo, B., Wu, Y., Zhao, Y., Lin, H., Ye, B., Michalski, J. R., Li, Y., Tai, K., Li, C., Guo, Z., Qi, C., Liu, S., Li, X. & Liu, J. (2023). Space weathering effects and potential spectral alteration on Phobos and the moon: clues

from the FE content of Olivine. *Astronomy and Astrophysics*, *672*, A115. https://doi.org/10.1051/0004-6361/202245453

Supporting Information for

MoonIndex, an Open-Source Tool to Generate Spectral Indexes for the Moon from M3 Data

Javier Eduardo Suárez-Valencia[1], Angelo Pio Rossi[1], Francesca Zambon[2], Cristian Carli[2], and Giacomo Nodjoumi[1]

[1]School of Science, Constructor University, Bremen, Germany, [2]INAF-Istituto Nazionale di Astrofisica, Italy.

Contents of this file

Introduction

In this supplementary material we detail the preparation of the data before being ingested to ***MoonIndex***, and the libraries used in python to generate the spectral indexes. Since the code to process the data in ISIS is not included on ***MoonIndex***, we will show the workflow we followed to map-project the images. Furthermore, we showcase 24 indexes resulting from our workflow, we show only the images obtained by the convex hull continuum-removal method, since it was the one used in the main text. For an explanation about the meaning of the indexes, refer to **Table 1** in the main text. The map-projected M^3 data cubes and the resulting indexes for the Apollo basin, Vallis Alpes, and Aristarchus crater can be found in this zenodo repository: https://zenodo.org/records/10014564.

Text S1.

The preprocessing of the data in ISIS consists on the map-projection of the cubes to a predefined coordinate system. ISIS does not recognize the higher-processed reflectance cube as an input, so the radiance cubes and associated files also need to be used. Before the projection could be done, we changed the name of the radiance cube by the one of the reflectance cube in the LBL file, this is done in the "^RDN_IMAGE" parameter under the "/* Spectral calibration parameters and radiometric gain factor data */" section of the file (**Figure S2**).

```
55
56 /* Spectral calibration parameters and radiometric gain factor data */
57
58 CH1:SPECTRAL_CALIBRATION_FILE_NAME      = "M3G20081211_RDN_SPC.TAB"
59 CH1:RAD_GAIN_FACTOR_FILE_NAME           = "M3G20081211_RDN_GAIN.TAB"
60 CH1:GLOBAL_BANDPASS_FILE_NAME           = "M3G20081211_RDN_BPF.IMG"
61
62 /* Description of Radiance-corrected image file */
63
64 OBJECT          = RDN_FILE
65   ^RDN_IMAGE    = "M3G20090204T192552_V03_RDN.IMG"
66   RECORD_TYPE   = FIXED_LENGTH
67   RECORD_BYTES  = 103360
68   FILE_RECORDS  = 18593
69
70   OBJECT                     = RDN_IMAGE
71     LINES                    = 18593
72     LINE_SAMPLES             = 304
73     SAMPLE_TYPE              = PC_REAL
74     SAMPLE_BITS              = 32
75     UNIT                     = "W/(m^2 um sr)"
76     BANDS                    = 85
77     BAND_STORAGE_TYPE        = LINE_INTERLEAVED
78     LINE_DISPLAY_DIRECTION   = DOWN
79     SAMPLE_DISPLAY_DIRECTION = RIGHT
80   END_OBJECT                 = RDN_IMAGE
81
82 END_OBJECT = RDN_FILE
83
```

Replace by the name of the reflectance cube

Figure S1. Replacement of names on the radiance LBL file.

Listing all files to do the batch processing

```
ls *V03_L1B.LBL | sed s/_L1B.LBL// > Imputs.lis
```

Transformation from IMG to cubes

```
chan1m32isis from=\$1_L1B.LBL loc=\$1_LOC.IMG obs=\$1_OBS.IMG
             to=\$1.cub -batchlist=Imputs.lis
```

Actualization of cubes kernels

```
spiceinit from=\$1.cub -batchlist=Imputs.lis
```

Making a new list

```
ls *V03.cub | sed s/.cub// > Imputs2.lis
```

Map projection, a map template need to be previously created

```
cam2map from=\$1.cub map=M3.map to=\$1_lv2.cub PIXRES=map -
                batchlist=Imputs2.lis
```

Strecth

```
stretch from=\$1_lv2.cub to=\$1_lv2_nonull.cub NULL=65535 -
                batchlist=Imputs2.lis
```

Once the replacement has been done, the full processing on ISIS and GDAL can be done with the following bash commands:

Listing all files

```
ls *.cub | sed s/.cub// > Imputs.lis
```

Translate

```
for f in *_nonull.cub; do
gdal_translate -a_nodata 65535 "$f" "${f%.*}.tif"
done
```

Once these commands have been run, the cubes will be projected and in .TIF format, and ready to ingest on ***MoonIndex***.

Text S2.

We used several python libraries during our workflow. Here we will discuss the application of all of them, and the full code can be access via the GiHub repository (https://github.com/Javierunal16/MoonIndex).

Preparation: During the preparation we used *rioxarray* to open the data cubes, and *numpy* to open the text file with the wavelengths for each M^3 channel. Then, *matplotlib.patches* is required to clip the cube to the desired extend, and *matplotlib.pyplot* to graph the data. In the RGB composites we used *sklearn.preprocessing* to normalize the values before plotting.

Filtering: To filter the cube we rely on libraries designed for image processing. First, *cv2* and *numpy* were needed to apply the Fourier filtration. And later, *numpy*, *specutils* and *astropy* were used to apply the 1D Gaussian filter.

Continuum removal: We tried several option to apply the convex hull to the spectra, but we ended up using *numpy* an *scipy.signal* to find the midpoint and to calculate the convex hull. As for the linear fit method, only *numpy* was needed.

Indexes generation: The creation of indexes is straighforward after the continuum removal, the majority of them require band operations that can be covered by *numpy*.

Deployment: The code was compiled using *wheel* and uploaded to PyPI with *twine*.

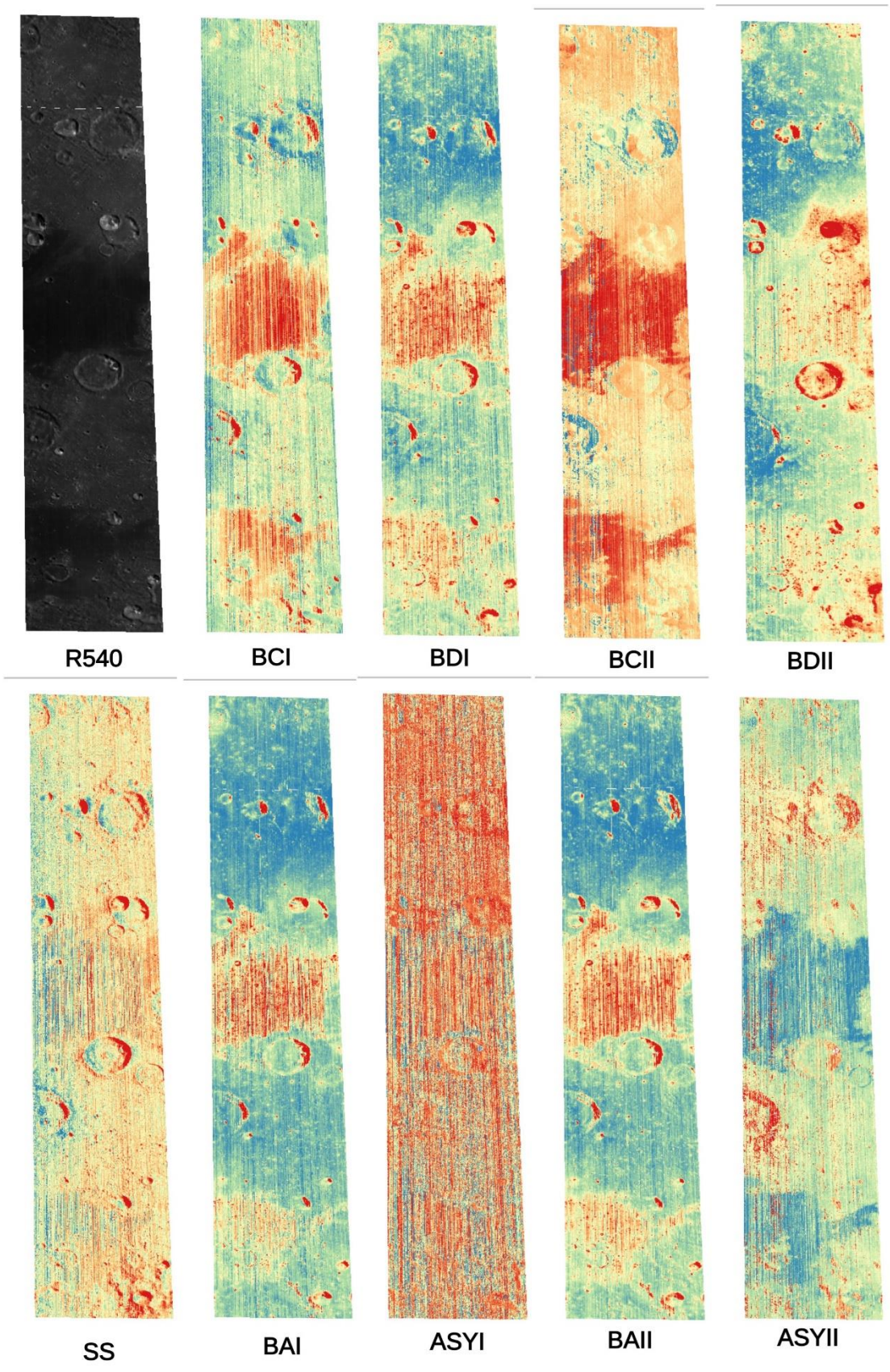
R540
BCI
BDI
BCII
BDII
SS
BAI
ASYI
BAII
ASYII

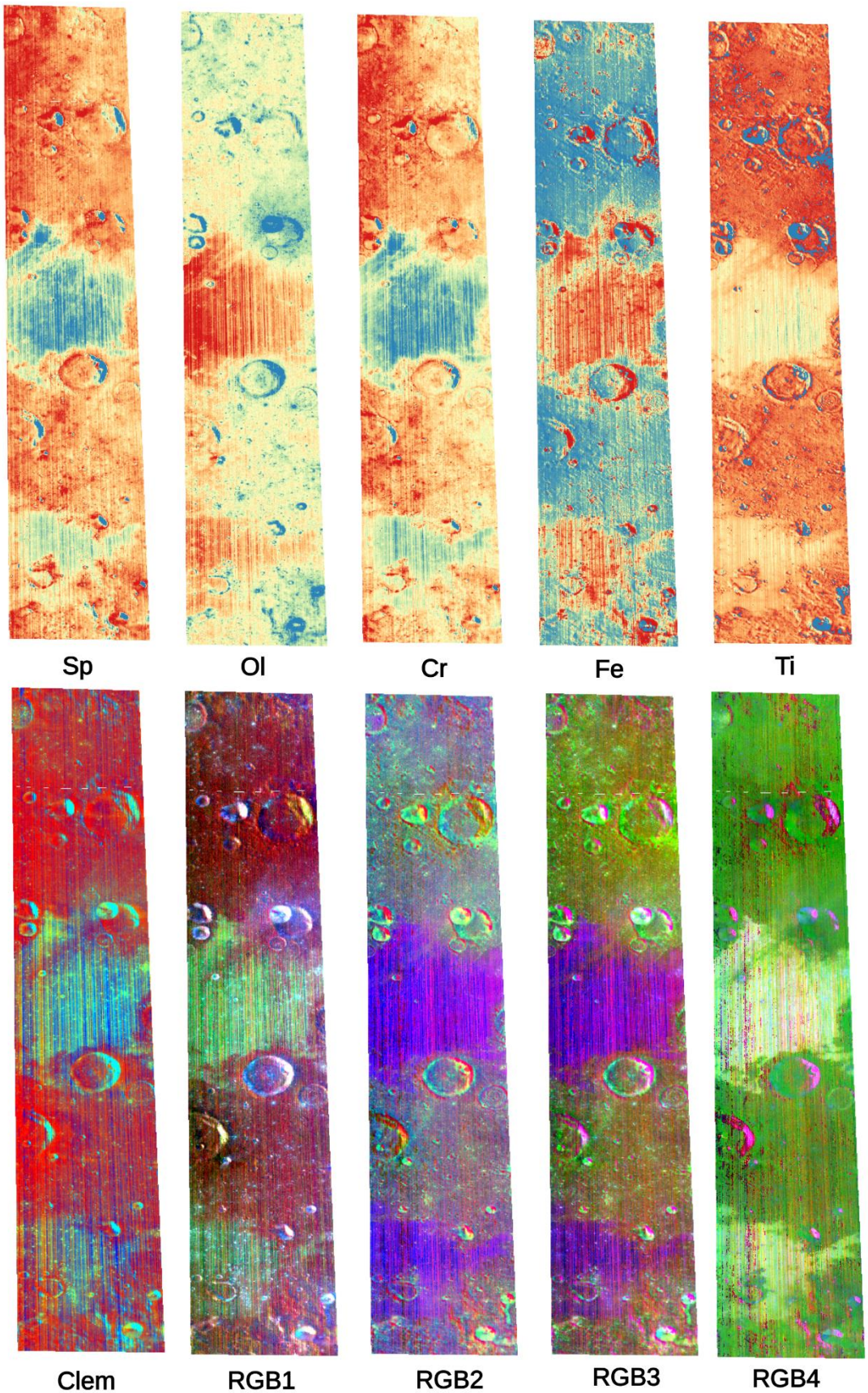

1076

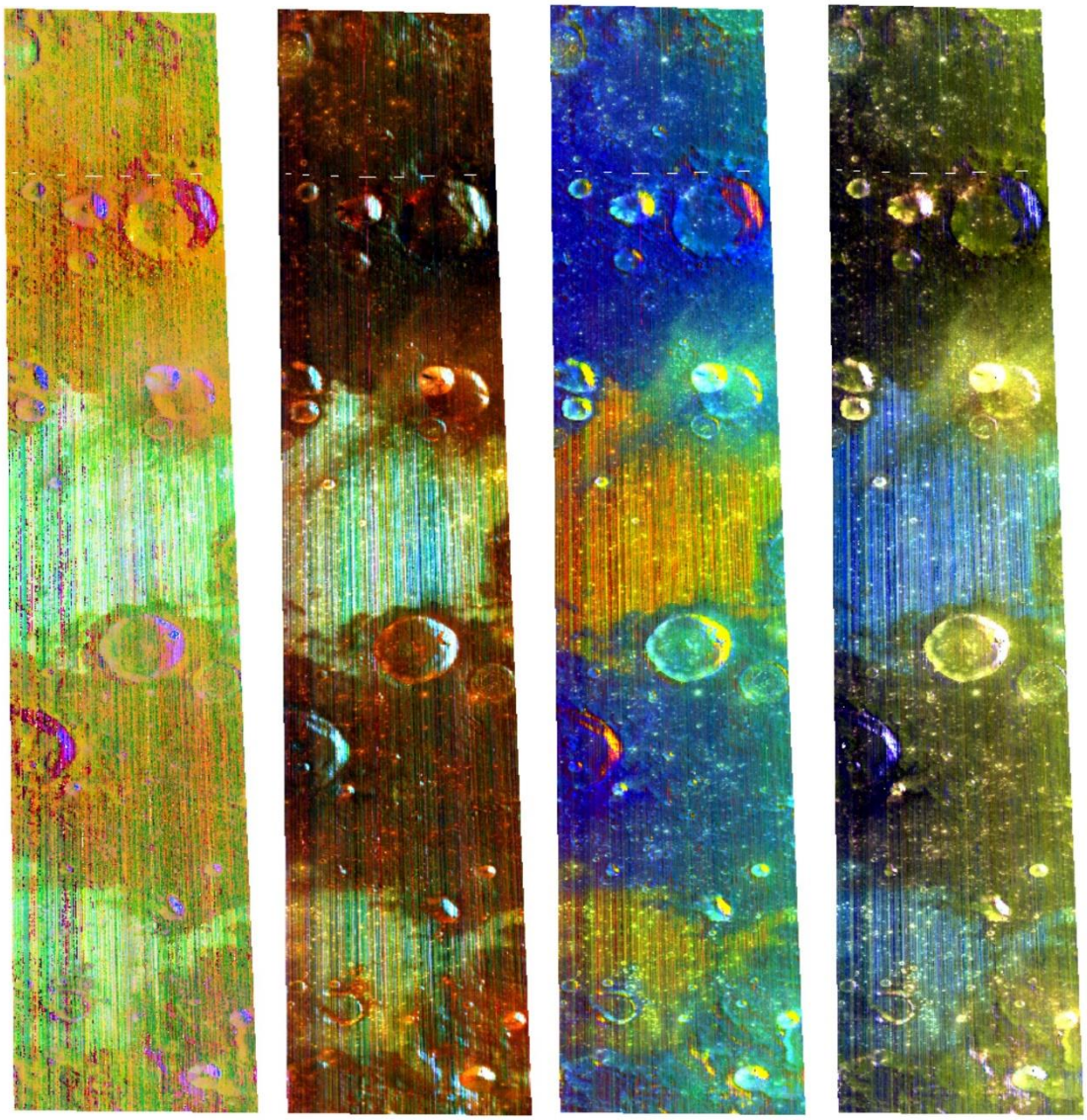

Figure S2. Spectral indexes derived from ***MoonIndex*** in the Apollo basin, using the convex-hull method.